Cell

Resource

Multimodal charting of molecular and functional cell states via *in situ* electro-sequencing

Graphical abstract

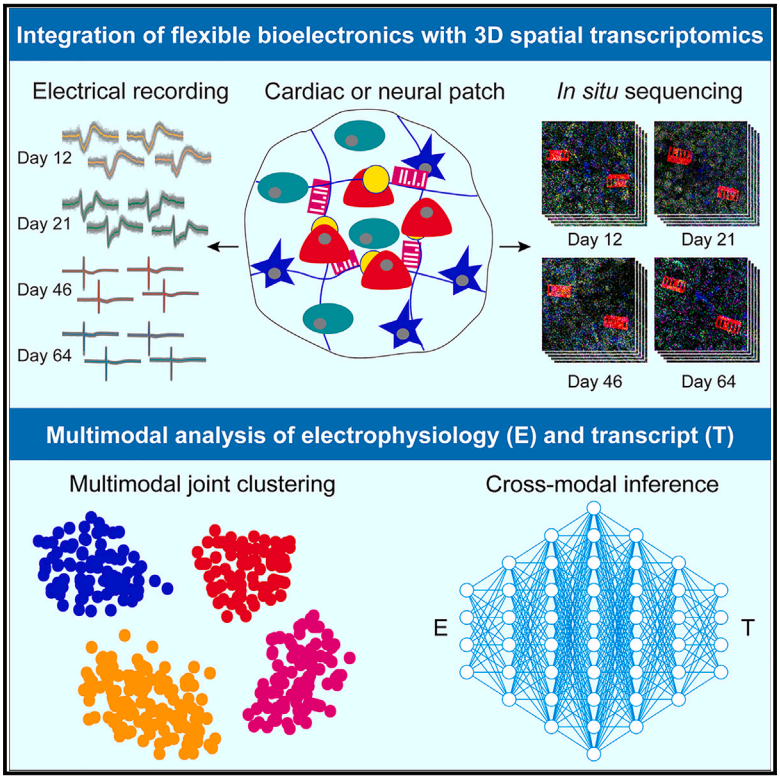

Authors

Qiang Li, Zuwan Lin, Ren Liu, ..., Ling Xiao, Xiao Wang, Jia Liu

Correspondence

xwangx@mit.edu (X.W.), jia_liu@seas.harvard.edu (J.L.)

In brief

Combined flexible bioelectronics with *in situ* RNA sequencing enables chronic electrophysiological recording and gene expression profiling in the same cells from cardiac and neural patches of cell assemblies or organoids, which facilitates identification of gene-to-electrophysiology relationships.

Highlights

- Integration of flexible bioelectronics with 3D spatial transcriptomics
- Paired identification of molecular and functional cell states
- Enabling *in situ* multimodal single-cell biology in intact biological networks
- Cross-modal inference between gene expression and electrophysiology

Li et al., 2023, Cell *186*, 2002–2017
April 27, 2023
https://doi.org/10.1016/j.cell.2023.03.023

CellPress

CellPress

Cell

Resource

Multimodal charting of molecular and functional cell states via *in situ* electro-sequencing

Qiang Li,[1,7] Zuwan Lin,[2,3,7] Ren Liu,[1,7] Xin Tang,[1,2,7] Jiahao Huang,[2,4] Yichun He,[1,2] Xin Sui,[2,4] Weiwen Tian,[1] Hao Shen,[1] Haowen Zhou,[2] Hao Sheng,[1] Hailing Shi,[2,4] Ling Xiao,[5,6] Xiao Wang,[2,4,*] and Jia Liu[1,8,*]

[1]John A. Paulson School of Engineering and Applied Sciences, Harvard University, Boston, MA 02134, USA
[2]Broad Institute of MIT and Harvard, Cambridge, MA 02142, USA
[3]Department of Chemistry and Chemical Biology, Harvard University, Cambridge, MA 02138, USA
[4]Department of Chemistry, Massachusetts Institute of Technology, Cambridge, MA 02139, USA
[5]Cardiovascular Research Center, Massachusetts General Hospital and Harvard Medical School, Boston, MA 02114, USA
[6]Cardiovascular Disease Initiative and Precision Cardiology Laboratory, Broad Institute of MIT and Harvard, Cambridge, MA 02142, USA
[7]These authors contributed equally
[8]Lead contact
*Correspondence: xwangx@mit.edu (X.W.), jia_liu@seas.harvard.edu (J.L.)
https://doi.org/10.1016/j.cell.2023.03.023

SUMMARY

Paired mapping of single-cell gene expression and electrophysiology is essential to understand gene-to-function relationships in electrogenic tissues. Here, we developed *in situ* electro-sequencing (electro-seq) that combines flexible bioelectronics with *in situ* RNA sequencing to stably map millisecond-timescale electrical activity and profile single-cell gene expression from the same cells across intact biological networks, including cardiac and neural patches. When applied to human-induced pluripotent stem-cell-derived cardiomyocyte patches, *in situ* electro-seq enabled multimodal *in situ* analysis of cardiomyocyte electrophysiology and gene expression at the cellular level, jointly defining cell states and developmental trajectories. Using machine-learning-based cross-modal analysis, *in situ* electro-seq identified gene-to-electrophysiology relationships throughout cardiomyocyte development and accurately reconstructed the evolution of gene expression profiles based on long-term stable electrical measurements. *In situ* electro-seq could be applicable to create spatiotemporal multimodal maps in electrogenic tissues, potentiating the discovery of cell types and gene programs responsible for electrophysiological function and dysfunction.

INTRODUCTION

Paired charting of single-cell gene expression and electrophysiology in intact cells and tissues across time and space is crucial to understanding gene-to-function relationships in fields ranging from developmental biology to cardiology and neuroscience.[1–5] Such multimodal methods require stable and continuous recording of individual cell electrical activity with high spatiotemporal resolution across three-dimensional (3D) biological samples, multiplexed profiling of a large number of genes in electrically recorded cells, and multimodal and cross-modal computational analysis.

Large-scale single-cell electrical recording[6–8] and high-throughput single-cell sequencing[9–11] have enabled system-level investigation of single-cell electrophysiology and gene expression, respectively. However, existing multimodal methods either lack high spatiotemporal resolution or cannot chronically stably measure electrical activities across 3D biological samples. For example, combining calcium imaging with RNA hybridization[12] reveals the correlation between calcium activity and molecularly defined cell types but only permits the recording of cell activity on the scale of seconds and profiling of a limited number of genes. On the other hand, patch-sequencing (patch-seq) method[1,3] quantifies cell activity with millisecond resolution and profiles the transcriptomes of recorded cells, but it assays cells one at a time and requires membrane disruption for electrical measurement, precluding 3D multiplexed and long-term stable electrical activity mapping.

Recent progress in thin-film flexible bioelectronics has enabled the development of flexible and stretchable "tissue-like" electronics capable of seamlessly integrating with tissue networks for long-term, stable, millisecond-timescale, single-cell electrical mapping.[13–17] Meanwhile, current imaging-based *in situ* sequencing methods[18] can achieve end-point spatial analysis of thousands of genes at subcellular resolution across intact biological samples. Here, we combine flexible and stretchable tissue-like bioelectronics with *in situ* sequencing in a method termed "*in situ* electro-sequencing (electro-seq)" that enables scalable and paired profiling of single-cell gene expression and electrophysiology in intact biological networks, including human-induced pluripotent stem cell (hiPSC)-derived cardiac patches and cultured mouse neural patches.

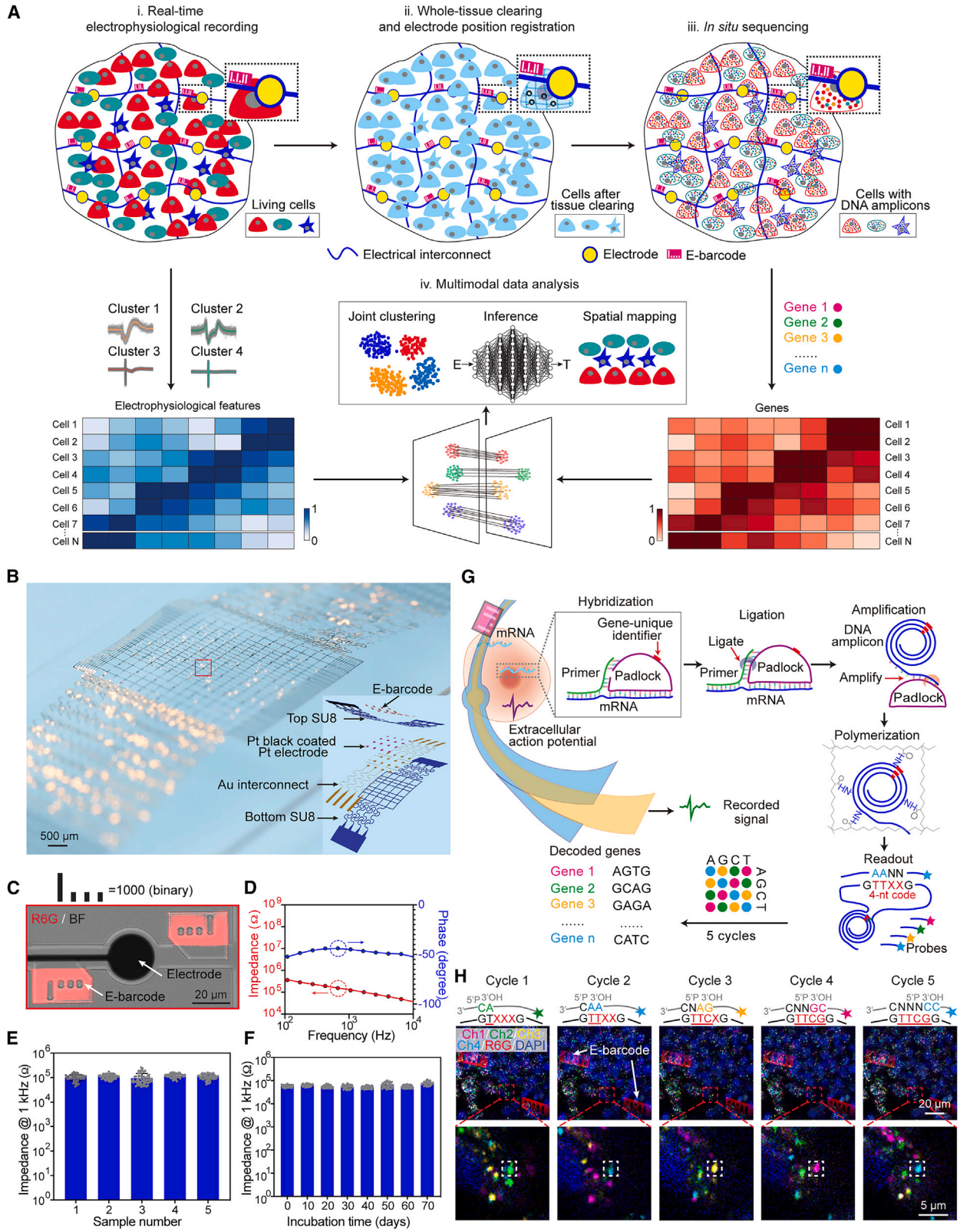

(legend on next page)

RESULTS

In situ electro-seq platform

We applied stretchable sub-micrometer-thick mesh electronics with cellular size electrodes to seamlessly integrate with cardiac and neural patches for continuous electrical recording and to prevent potential cell-to-electrode dislocation during cell culture, sample preparation, and multiple cycles of *in situ* sequencing (Figure 1A). Then, we embedded the sample into a hydrogel to form a cell-electronics-hydrogel network that is compatible with the *in situ* sequencing protocol and capable of co-deformation during volume change. To precisely identify the electrically recorded cells in 3D cell networks, we used photolithography to pattern the thin-film microscale polymeric structures with distinct fluorescent electronic barcodes (E-barcodes), which were paired with each individual electrode to label its recording channel during fluorescence imaging cycles of *in situ* sequencing. The E-barcodes served to trace each electrode and identify the electrically recorded cells with precise 3D coordinates, allowing for the integration of electrical recording with gene expression.

Briefly, *in situ* electro-seq consists of four key steps (Figure 1A): (1) the mesh electronics with E-barcoded electrodes are embedded in the biological samples, such as cardiac and neural patches for continuous electrical recording; (2) the entire cell-electronics hybrid is fixed, embedded in hydrogels, and cleared for *in situ* sequencing; (3) gene identities and E-barcodes are simultaneously read out by multiple cycles of fluorescence imaging to integrate electrical recording with gene expression profiling at single-cell resolution; and (4) the integrated data are analyzed using multimodal and cross-modal visualization and correlation to reconstruct spatiotemporal gene-to-function relationships.

In situ electro-seq integrates single-cell transcriptional and electrophysiological states of hiPSC-derived cardiac patches

We applied *in situ* electro-seq to hiPSC-derived cardiomyocyte (hiPSC-CM) patches to map electrophysiology and gene expression from the same cells. First, our representative mesh electronics had 64 electrodes, each 25 μm in diameter (Figures 1B and S1), and were designed, based on recent reports,[6,7,19–22] to record localized, single-cell-level electrophysiology[19,21] with low noise level (root mean square voltage < 10 μV) and reliable single-unit separation (amplitude > 60 μV). A pair of center-symmetric fluorescent E-barcodes with distinct binary codes was patterned with each electrode at the center (Figures 1C, S1F, and S1G). Characterizing electrode impedance (Figure 1D) showed stable performance across different samples (Figure 1E) and over 2 months in the physiological solution (Figure 1F) for long-term electrical recording.

Then, hiPSC-CMs were generated and integrated with mesh electronics to form a cardiac patch, as described previously.[14,17] We used immunostaining and calcium imaging to characterize the quality of hiPSC-CMs (Figures S2A and S2B). The immunostaining results showed that approximately 95% of the cells were CMs marked by troponin T (TNT), α-actinin, myosin heavy chain 6 (MYH6), and hyperpolarization-activated cyclic nucleotide-gated cation channel 4 (HCN4), demonstrating that our protocol generated hiPSC-CMs with high purity and little batch-to-batch variation (Figures S2C and S2D). The calcium imaging results further showed that the calcium waveform kept evolving from day 12 to 21 and stabilized from day 21 to 64 (Figures S2E–S2I), consistent with previous findings.[23] After co-culturing hiPSC-CMs with mesh electronics, we immunostained TNT and α-actinin on hiPSC-CM patch-electronics hybrids. Results demonstrated that the integrated mesh electronics had negligible effects on hiPSC-CM development (Figures S2J–S2R). Finally, we fixed hiPSC-CM patch-electronics hybrids and applied the *in situ* sequencing protocol (see STAR Methods) to spatially profile a targeted set of cardiac genes, including the 201 most differentially expressed genes during cardiac development, extracted from the previous single-cell RNA sequencing (scRNA-seq) data.[24–27] Specifically, RNA-derived DNA amplicons with pre-designed gene-specific identifiers were synthesized *in situ* by probe hybridization, enzymatic amplification, and immobilization in the cleared hiPSC-CM patch-electronics-hydrogel network (Figure 1G), and gene-specific identifiers were then decoded through five sequencing cycles.[18] To evaluate potential cell-to-electrode dislocation during sample preparation and multiple cycles of *in situ* sequencing, we calculated the change in the distances from cells to electrodes before and after sample preparation to be 0.51 ± 0.43 μm, which is orders of magnitude smaller than the size of one cell, and thus negligible (Figures S3A–S3D). Additionally, the microscale distances among E-barcodes, cells, and amplicons remained unchanged during the multiple cycle imaging (Figure 1H).

Next, we tested *in situ* electro-seq in the hiPSC-CM patches (Figures 2A–2D). The electrical recording was performed, and single-spike field potential waveforms were identified, pre-processed, averaged, and down-sampled to extract features. Figures 2E and 2F show representative voltage traces and single-spike waveforms, respectively. The uniform manifold approximation and projection (UMAP)[28] visualization (Figure 2F, inset) of extracted features from each channel showed the heterogeneity of hiPSC-CM electrophysiology. We also used drug

Figure 1. *In situ* electro-seq platform

(A) Schematics summarizing the *in situ* electro-seq method.

(B) Representative photograph of flexible mesh electronics. Inset: schematic illustrates the multilayer structure of the electronics.

(C) Overlapped fluorescence and bright-field (BF) image of a pair of binary E-barcodes highlighted in red box in (B).

(D) Electrochemical impedance and phase from 0.1 to 10 kHz of a representative electrode.

(E and F) Electrochemical impedance at 1 kHz across five different samples (E) and over 2 months of incubation (F). Values are mean ± SEM.

(G) *In situ* sequencing of a cell-electronics hybrid (see STAR Methods).

(H) Representative images of five rounds of sequencing overlaid with E-barcode. X, unknown base; red underline, decoded sequence; Ch1 to Ch4, fluorescence channels; E-barcodes labeled with R6G.

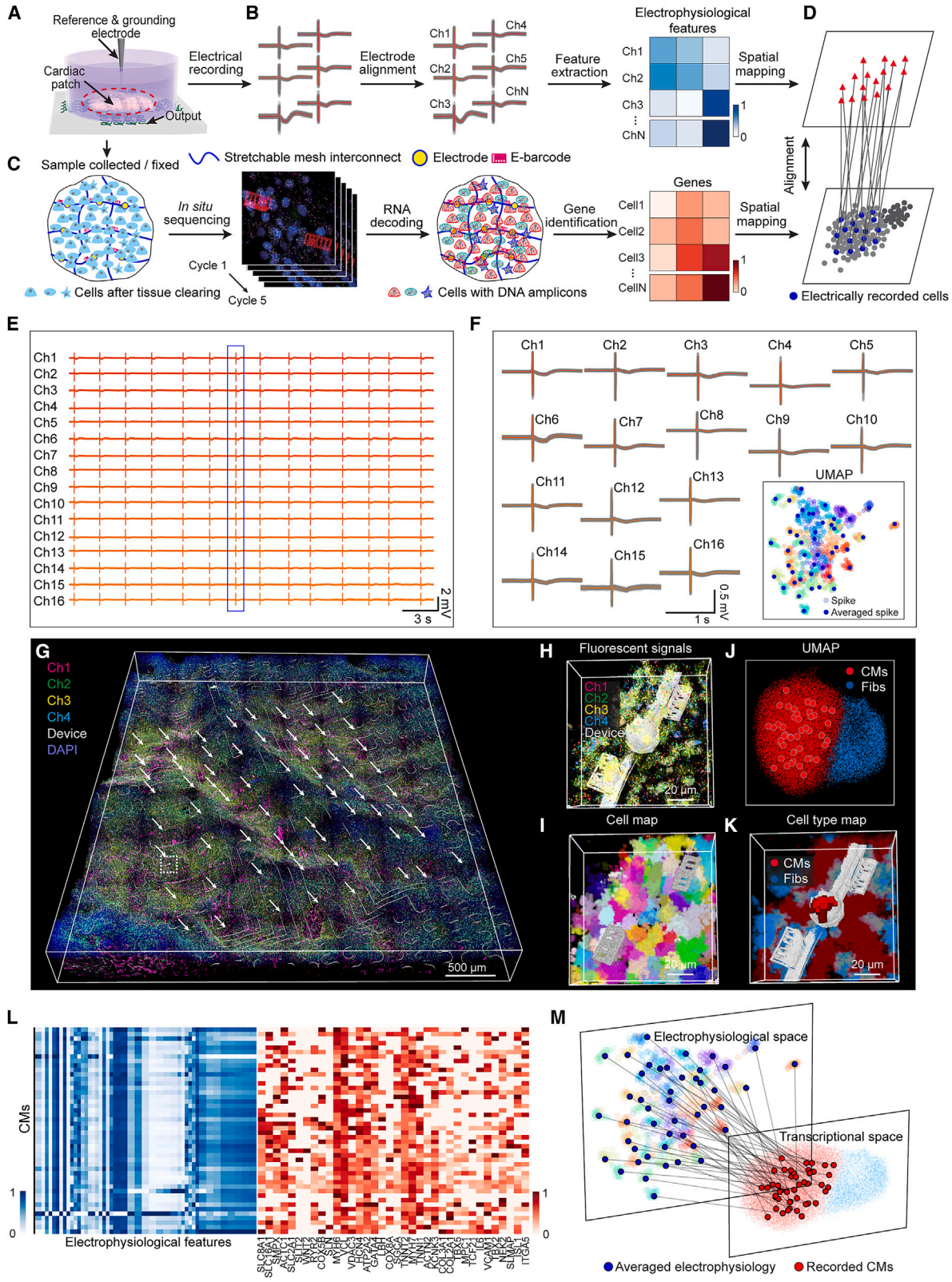

(legend on next page)

tests to confirm that the mechanical activities of hiPSC-CMs cause no interruptions on the electrical recording (Figures S3E–S3H). Then, *in situ* sequencing was applied immediately after electrical recording (Figure 2G). After 3D cell segmentation (Figures 2H and 2I),[29] we performed cell clustering by Leiden clustering.[30] The result showed two major cell types (Figure 2J), CMs and cardiac fibroblasts (Fibs), which were spatially mapped back to E-barcoded electrodes (Figure 2K).

To determine how to identify the cells recorded by the electrodes, we conducted electrical recording and calcium imaging in the same sample (Figures S3I–S3L) and tested the localization of signals recorded from the mesh electronics. The results indicated that, among all calcium signal-positive cells, only those that directly contact electrodes can be recorded (Figure S3L). Based on this data, we first built a computational pipeline to automatically identify CMs that directly contact the electrode as electrically recorded cells (Figures 2K, S3M, and S3N). Then, the identification of E-barcodes registered the electrophysiological features (E features) with gene expression of the electrically recorded cells. The resulting heatmap (Figure 2L) and joint UMAP (Figure 2M) visualizations showed the integrated E features with the differentially expressed CM-related genes and their multimodal distributions, respectively.

In situ electro-seq enables the multimodal spatial mapping of neural patches

We applied the *in situ* electro-seq to neural patches by first integrating stretchable mesh electronics with sparsely seeded primary mouse hippocampal neurons (Figure 3A). The electrical recordings of single-neuron activity showed high heterogeneity in their temporal firing patterns and spike waveforms (Figures 3B, 3C, and S4B). *In situ* sequencing was performed after electrical recording. After 3D cell segmentation, we performed cell clustering by Leiden clustering. The results showed five major cell types (Figures 3F, S4C, and S4D): excitatory neurons, inhibitory neurons, astrocytes, Fibs, and glial cells, all of which were then spatially mapped back to their locations (Figure 3D). To ensure correct identification of the electrically recorded neurons, we considered only two scenarios: (1) only one neuron within 60-μm of the corresponding electrode (the sensing area), or (2) the same neural signal simultaneously captured by multiple electrodes. Next, we performed spike sorting and identified the neuron locations using electrode positions and corresponding spike amplitudes, as previously described (Figures 3E and S4A).[31] The sparse distribution of seeded neurons among glial cells enabled robust identification of the electrically recorded neurons at single-cell resolution. The electrical waveforms were then mapped to the associated electrically recorded neurons (Figure 3E). Notably, we observed distinct gene expression patterns between electrically recorded excitatory and inhibitory neurons, with excitatory neurons showing high expression of *Slc17a6* and inhibitory neurons showing high expression of *Gad1* (Figures 3G, S4C, and S4D). Furthermore, by correlating the cell type with electrical recording, we found that excitatory and inhibitory neurons show a statistically significant difference in electrical features such as peak-trough ratio (Figures 3G and 3H), which is consistent with the previous reports.[32,33] Together, these results demonstrated that the *in situ* electro-seq platform is capable of correlating cell electrophysiology and gene expression at the single-cell level when applied to cultured neural networks.

In situ electro-seq enabled multimodal joint clustering

We used *in situ* electro-seq to trace the development of hiPSC-CM patches (Figure 4A). The cell electrophysiological signals from days 12, 21, 46, and 64 of differentiation (Figures 4B and 4C) showed distinct features at these four stages. We next applied the ClusterMap[29] method to segment cells based on RNA identities. UMAP visualizations of cell types across four differentiation stages showed equivalent embedding distributions between electronics-contacted and control cells, suggesting the negligible effects of mesh electronics on hiPSC-CM development and on the performance of *in situ* sequencing (Figures 4D and 4E). We then performed Leiden clustering analysis on all *in situ* sequenced samples across 4 stages and identified 5 cell clusters (Figure 4F). Based on the expression levels of marker genes, four clusters can be characterized as CMs and one as cardiac Fibs. Moreover, based on previous reports,[24,34] the changing expression levels of marker genes (e.g., *HCN4*, *MYH6*, *MYH7*, *MYL7*, *MYL4*, etc.) in these four types of CMs indicated a transition from nodal-like through atrial-like to ventricular-like CMs (Figures 4G and 4H). Notably, the nodal marker gene (*HCN4*) and atrial marker gene (*MYH6*) decreased at later stages, while the ventricular maker gene (*MYH7*) increased (Figures 4I and 4J).

While gene expression clustering separates hiPSC-CMs into four transcriptional states (t-states) that roughly correspond to the samples collected at the four differentiation days, we noticed

Figure 2. *In situ* electro-seq integrates single-cell transcriptional and electrophysiological states of hiPSC-CM patches

(A–D) Schematics illustrating *in situ* electro-seq of a hiPSC-CM patch.

(E) Representative voltage traces recorded from the hiPSC-CM patch at day 46 of differentiation. The data is also included in Figure 4B to show the overall cardiac electrophysiological activity changes from day 12 to day 64.

(F) Representative averaged single-spike waveform detected from (E) and highlighted in the blue box. Inset shows the UMAP visualization of the spike waveforms. The data is also included in Figure 4C to show the overall cardiac electrophysiological activity changes from day 12 to day 64.

(G) 3D reconstructed fluorescence imaging of in-process *in situ* electro-seq of the entire hiPSC-CM patch-electronics hybrid. White arrows highlight the positions of electrodes.

(H) Zoomed-in view of the fluorescent signals illustrating the representative electrode-embedded area from the white dashed box in (G).

(I) 3D cell segmentation map labeling cells with different colors.

(J) UMAP visualization representing major cell types across all sequenced cells clustered by Leiden clustering. The electrically recorded cells are highlighted.

(K) 3D cell-type map labeling each cell by its cell type with the same color code in (J). The electrically recorded cell is highlighted with deep red.

(L) Heatmap of the normalized electrophysiological features (blue) and differentially expressed genes (red) from the measured cells.

(M) Integration of electrophysiological features with gene expression features in UMAP visualizations.

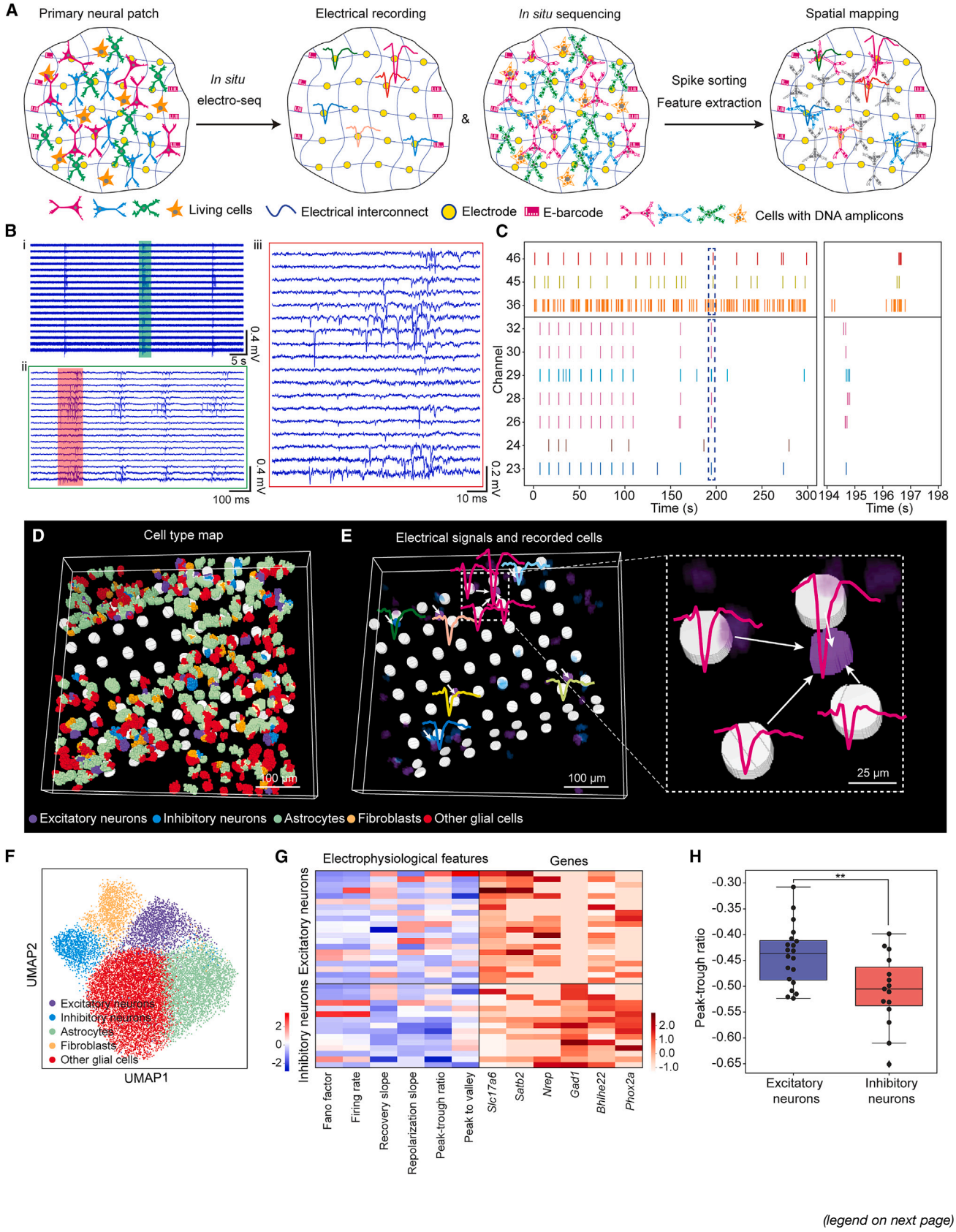

(legend on next page)

that CM t-states at days 46 and 64 of differentiation are less separable (Figure 4F). Statistical testing showed that the separability of t-states of electrically recorded hiPSC-CMs was worse (Figures 5A, S5A, and S5B) for days 21, 46, and 64 of differentiation (Figures S5C and S5D), agreeing with previously reported scRNA-seq clustering of hiPSC-CM t-states during development.[24] Using E features to cluster the electrically recorded cells, we identified two major electrophysiological states (e-states) for hiPSC-CMs, one for days 12 and 21, and the other for days 46 and 64. However, the separability of subgroups within the two major groups was low (Figures 5B and S5E). Previous patch-seq results suggested that integrating gene expression with electrophysiology could improve the classification of cell types.[35] Thus, we used the weight nearest neighbor (WNN)[36] algorithm from *Seurat* v4 to integrate electrophysiological and gene expression data as joint representation (see STAR Methods). Using the joint features, hiPSC-CMs can be clustered into four joint states (j-states) that well represent the distinct differentiation days (Figures 5C and S5F). In addition, we applied *Monocle3*[37] to calculate pseudotime distributions of t-states, e-states, and j-states. The results also showed that integrating gene expression and electrophysiology data led to a better separation of pseudotime distributions for cells at distinct differentiation stages (Figure 5D). The electrically recorded hiPSC-CMs with their j-state pseudotimes were highlighted in the UMAP visualization of hiPSC-CM t-states (Figure 5E) to show that the j-states clearly recapitulated the continuous developmental trajectory of hiPSC-CMs (Figures 4E and 4I). Additionally, we investigated the contribution of non-transcriptional factors to electrophysiology, such as spatial information of cells and oscillator coupling between hiPSC-CMs. The results showed that these non-transcriptional factors also correlate with electrophysiology but to a much lower extent in comparison with the transcriptional factor (Figure S5G–S5J). Collectively, these data demonstrate that the *in situ* electro-seq platform can efficiently characterize the evolution of cell states over the time course of hiPSC-CM development.

In situ electro-seq enabled cross-modal correlation and inference

A capability of *in situ* electro-seq is the development of a model for cross-modal inference, which can be used to (1) infer gene expression at unmeasured time points from continuous electrophysiological measurements and (2) change the expression levels of individual genes or a combination of multiple genes to infer their effects on electrophysiology. To achieve this, we used sparse reduced-rank regression (RRR) analysis, a statistical model successfully applied to analyze patch-seq data,[38] to (1) quantitatively investigate the correlations between individual genes and changes in electrophysiological waveform features during hiPSC-CM differentiation and development, and (2) select a subset of genes that is most relevant to the temporal evolution of these electrophysiological waveform features throughout hiPSC-CM development (Figure 6A).

Specifically, we down-sampled the entire spike waveform and extracted data points (Figure 6B) directly from the waveform as input E features. Then, we plugged our paired electrophysiological and transcriptional measurements into the sparse RRR model, which aligned the electrophysiological and transcriptional representations in the low-dimensional space and generated two corresponding biplots (Figure 6C).[35,38] This allowed us to directly pinpoint the correlations between certain E features and certain gene transcripts by comparing the angles of projected lines (i.e., E features and gene transcripts, respectively) between the two biplots.[35,38] Next, we used the cosine distance as the metrics to evaluate the correlations between gene transcripts and E features in these biplots and generated a gene-to-E feature correlation heatmap (Figures 6D and 6E). We found that different genes correlated with different E features, which were grouped based on the quadrants of the electrophysiological biplot (Figure 6C). The analysis led to a distilled list of genes, whose temporal dynamics are most correlated with the temporal evolution of E features throughout hiPSC-CM development (Figure 6F). The model-selected genes include: (1) cardiac structural genes, such as myosin heavy chain (*MYH6*, *MYH7*), troponin complex (*TNNT2*), and Z-disc (*VCL*, *VIM*); (2) ion-channel-related genes, such as sodium-calcium exchangers (*SLC8A1*), calcium signaling gene (*RYR2*), and potassium channels (*KCND3*); and (3) metabolic genes, such as endoplasmic reticulum calcium transporting genes (*ATP2A2*) and cytochrome *c* oxidase subunit 8A (*COX8A*).

Next, to enable continuous electrophysiology-to-transcript (E-to-T) and transcript-to-electrophysiology (T-to-E) inferences, we constructed a coupled autoencoder[39,40] to learn coordinated representations of the E features and sparse RRR analysis-selected gene transcripts from days 12, 21, 46, and 64 of differentiation (Figure 7A). The coupled autoencoder consists of two autoencoder networks, each comprising an encoder and a decoder subnetwork that project the input E features or gene transcripts into a low-dimensional representation and back to the input data space. After learning the paired training data between E features and gene transcripts, the trained coupled

Figure 3. *In situ* electro-seq enables the multimodal spatial mapping of neural patches

(A) Schematics illustrating *in situ* electro-seq of neural patches.

(B) Representative voltage traces showing spike-bursting dynamics of mouse hippocampal neurons (i) with the bursting activity (ii) and single-spike train (iii) highlighted.

(C) Detected spike trains from continuous recording (left panel) and single spikes (right panel) from the dashed box highlighted region.

(D) Overlapped 3D cell-type and electrode maps. Gray color labels each individual electrode.

(E) Identified electrically recorded neurons. Colors label spikes identified from each neuron highlighted by white arrows. Zoomed-in image shows one neuron that was simultaneously recorded by four electrodes.

(F) UMAP visualizations of all the sequenced cells.

(G) Heatmap showing the normalized electrophysiological features and marker gene expression profiles.

(H) Box and dot plots showing the peak-trough ratio between excitatory and inhibitory neurons.

n = 20 for excitatory neurons, n = 15 for inhibitory neurons, ** $p < 0.01$, two-tailed, unpaired t test.

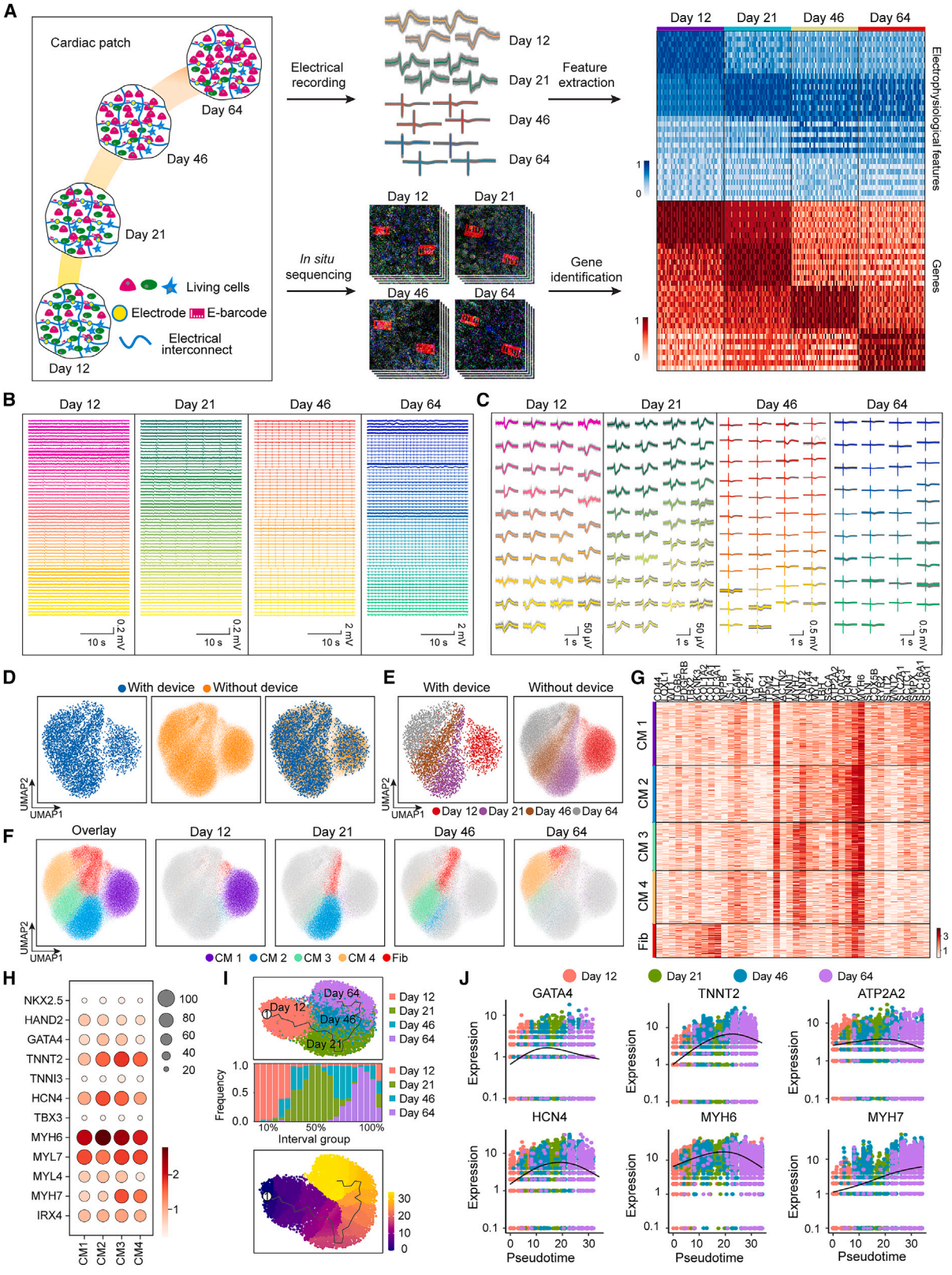

(legend on next page)

autoencoder was able to successfully project the high-dimensional transcriptional (*Xt*) and electrophysiological (*Xe*) data to aligned low-dimensional representations (*Zt* and *Ze*) (Figure 7B). This suggests that a common latent representation exists between the gene expression and electrophysiology modalities, and that we could potentially infer one modality from the other.[39,40] To test this, we applied the pre-trained coupled autoencoder to a validation dataset and successfully inferred transcriptional data from electrophysiological data (Figure 7C). 5-fold cross-validation showed high inference performance of the coupled autoencoder (Figures 7D–7F; STAR Methods). These results suggested that electrophysiological data generated by *in situ* electro-seq can be used to infer the expression of electrophysiology-related gene programs and vice versa.[39,40]

After confirming the performance of the model, we first applied the pre-trained coupled autoencoder to infer temporal gene expression change from the continuous electrical recording of the same sample (Figures 7G, S5M, and S5N). Because the gene expression measurement is an end-point measurement that requires sample fixation, it is difficult to directly measure temporal gene expression profiles from the same sample over the time course of development. However, our flexible electronics can record cell electrical activity from the same sample over a period of months. Then, our coupled autoencoder-based model offers the possibility of inferring a temporal gene expression profile from the long-term electrical recording of the same sample (Figure 7Gi). Specifically, Figures 7Gi–7Giii show that the electrical activity of a hiPSC-CM sample was measured by the embedded electrodes from day 17 to 64 of differentiation. A temporal gene expression profile from day 17 to 64 of differentiation was then inferred (Figures 7Giv and 7Gv). To validate the inferred result, we measured the gene expression from the sample after the long-term electrical measurement on the last day of recording—day 64 of differentiation. Comparing the measured gene expression with the inferred gene expression reveals a Pearson's r of 0.68 ± 0.11 (mean ± SD) (Figure 7Gv), which can be considered as good results based on previous studies.[35,39,41]

Finally, we applied the pre-trained coupled autoencoder model to dilated cardiomyopathy (DCM) patient-derived LMNA (lamin A/C protein) mutant cells.[42] We used the gene expression changes in LMNA-mutant hiPSC-CMs from previously reported data[42] to infer the electrophysiological waveform (Figures 7Hi–7Hiii). Compared with the electrophysiological waveform from healthy hiPSC-CMs, the inferred LMNA-mutant hiPSC-CM waveform showed distinct E features, including (1) missed sharp up/down stroke, (2) declined depolarization upstroke and repolarization downstroke amplitude in phase 0/1, and (3) increased afterdepolarization amplitude in phase 2/3 (Figures 7Hiv). To experimentally validate whether the inferred LMNA-mutant hiPSC-CM electrophysiological waveform can successfully recapitulate the real electrical activity of LMNA-mutant hiPSC-CMs, we cultured the LMNA-mutant hiPSC-CMs on the mesh electronics and recorded their electrical activities. The results showed that the inferred waveform aligned well with the measured waveform (Figure 7Hiv), with a Pearson's r correlation of 0.63 (Figure 7I). In contrast, the waveform inference results after random shuffling of LMNA-mutant hiPSC-CMs' gene expression showed a low Pearson's r correlation of −0.14 with the measured LMNA-mutant waveform (Figure 7I). These results provide further indication of the potential value of our model, specifically in the context of cardiac diseases, where the testing samples involve the same cell types to those used in the training samples.

We noted that current machine learning or statistical learning models for cross-modal inference were built solely on the training data. Such a model can achieve satisfactory inference results when the testing data has similar characteristics to the training data. For example, in this case, the LMNA-mutant hiPSC-CMs at a later developmental stage showed similar electrophysiological waveform characteristics to the training samples (healthy hiPSC-CMs) at early developmental stages, so our pre-trained coupled autoencoder model was still able to infer its electrophysiological waveform. However, we noted that the current machine-learning-based model may not be directly applied to infer electrophysiological waveforms of samples with characteristics substantially different from the training sample distribution. As a result, increasing the training datasets to cover a wider range of time points across longer development periods and more diverse hiPSC-CM samples (including different mutation and disease samples) may potentially improve the applicability of the model, particularly for inferring electrophysiological changes resulting from multiple gene expression changes in cardiac diseases, wherein testing samples involve identical cell types to those in the training data.

DISCUSSION

We demonstrate that *in situ* electro-seq is capable of integrating electrophysiology and gene expression at single- and multi-cell levels (Figures S6 and S7), providing (1) multimodal joint cell clustering for identification of cell states and trajectories, which cannot be directly traced by previous approaches, (2) cross-modal

Figure 4. *In situ* electro-seq enables multimodal tracing of cell states in hiPSC-CM development

(A) Overview schematics showing *in situ* electro-seq of hiPSC-CM patches at different developmental stages.

(B) Representative voltage traces recorded from the hiPSC-CM patches.

(C) Representative single-spike activities.

(D and E) UMAP visualizations of all electronics-contacted cells and control cells.

(F) UMAP visualizations highlighting the cell types clustered by Leiden clustering and their distributions.

(G) Heatmaps of normalized differentially expressed genes for each cell type.

(H) Dot plots of selected marker gene expressions.

(I) Top: UMAP visualizations showing the representative trajectory of hiPSC-CM development. Colors correspond to days of differentiation. Middle: stacked bar plot showing the percentage of cells across inferred pseudotime. Bottom: UMAP visualizations showing the representative trajectory of hiPSC-CM development. Colors correspond to inferred pseudotime.

(J) Kinetics plots showing relative expressions of marker genes.

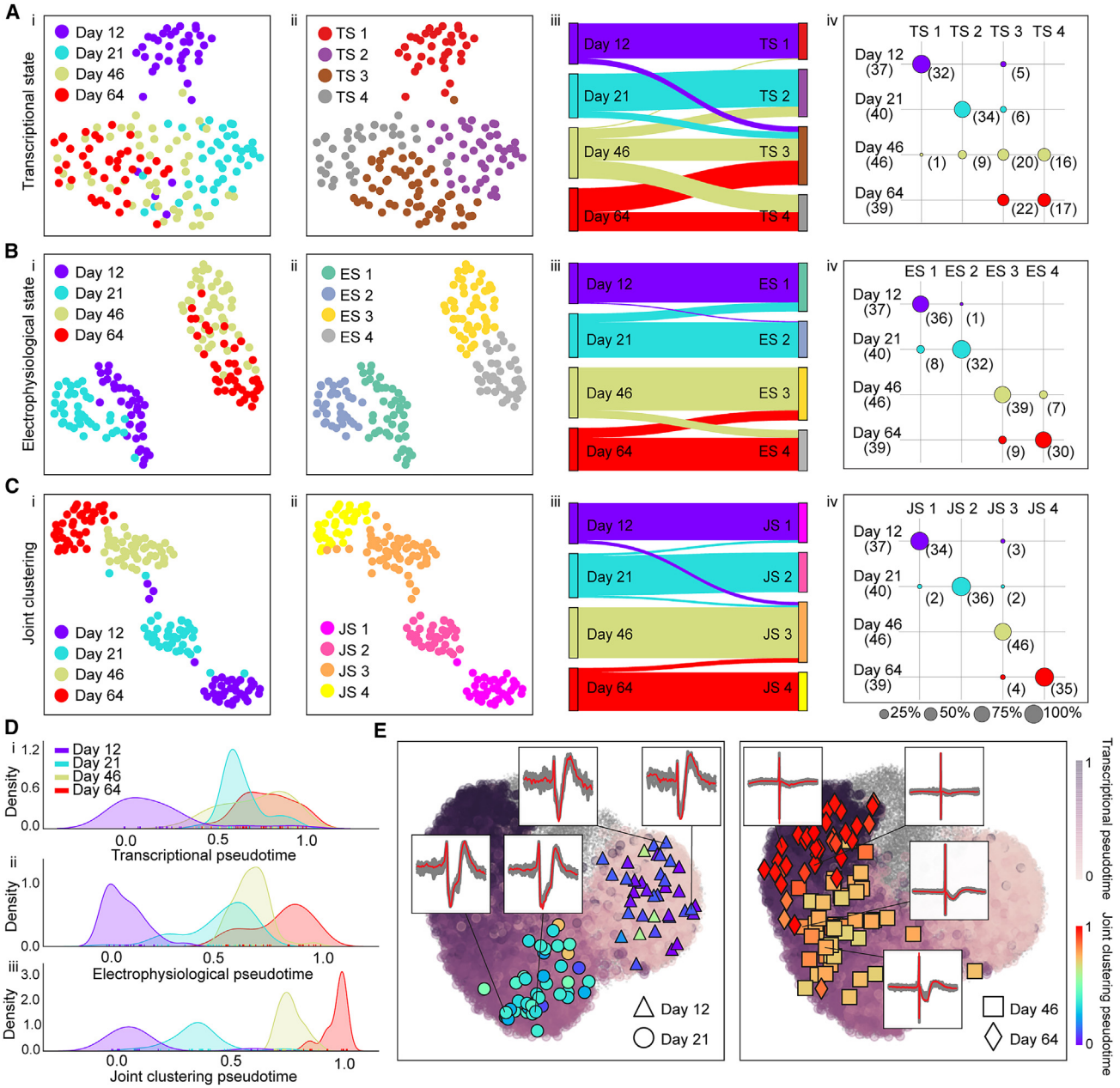

Figure 5. *In situ* electro-seq enables joint clustering of cell states in hiPSC-CM development

(A) hiPSC-CM transcriptional states (t-states, TS) defined by gene expression. UMAP visualization of gene expression of electrically recorded CMs, color-coded by differentiation days (i) and t-states defined by Leiden clustering (ii). Comparison of t-states and differentiation days by river plot (iii) and dot plot (iv).

(B) hiPSC-CM electrophysiological states (e-states, ES) defined by electrophysiology and analyzed in the same way as in (A).

(C) hiPSC-CM transcriptional and electrophysiological joint states (j-states, JS) defined by weighted nearest neighbor (WNN)-integrated representations from gene expression and electrophysiology and analyzed in the same way as in (A).

(D) Distribution plots showing pseudotime distributions of all the electrically recorded hiPSC-CMs. Gene expression (i), electrophysiology (ii), and WNN-integrated representations of gene expression and electrophysiology (iii).

(E) Electrically recorded cells highlighted in the UMAP visualization of gene expressions from all cells, with colors encoding joint pseudotime in (Diii). Cells sequenced from all the samples across four stages are shown as gray embedding (the same as Figure 4F). Insets show representative single-spike waveforms.

inference that uses continuous electrical measurements to infer cell gene expression profiles, and (3) identification of gene programs directly relevant to electrophysiology.

Our imaging and electrical data suggest that electrical signals are primarily recorded from the hiPSC-CMs that have the largest direct contact area with the electrode. However, we

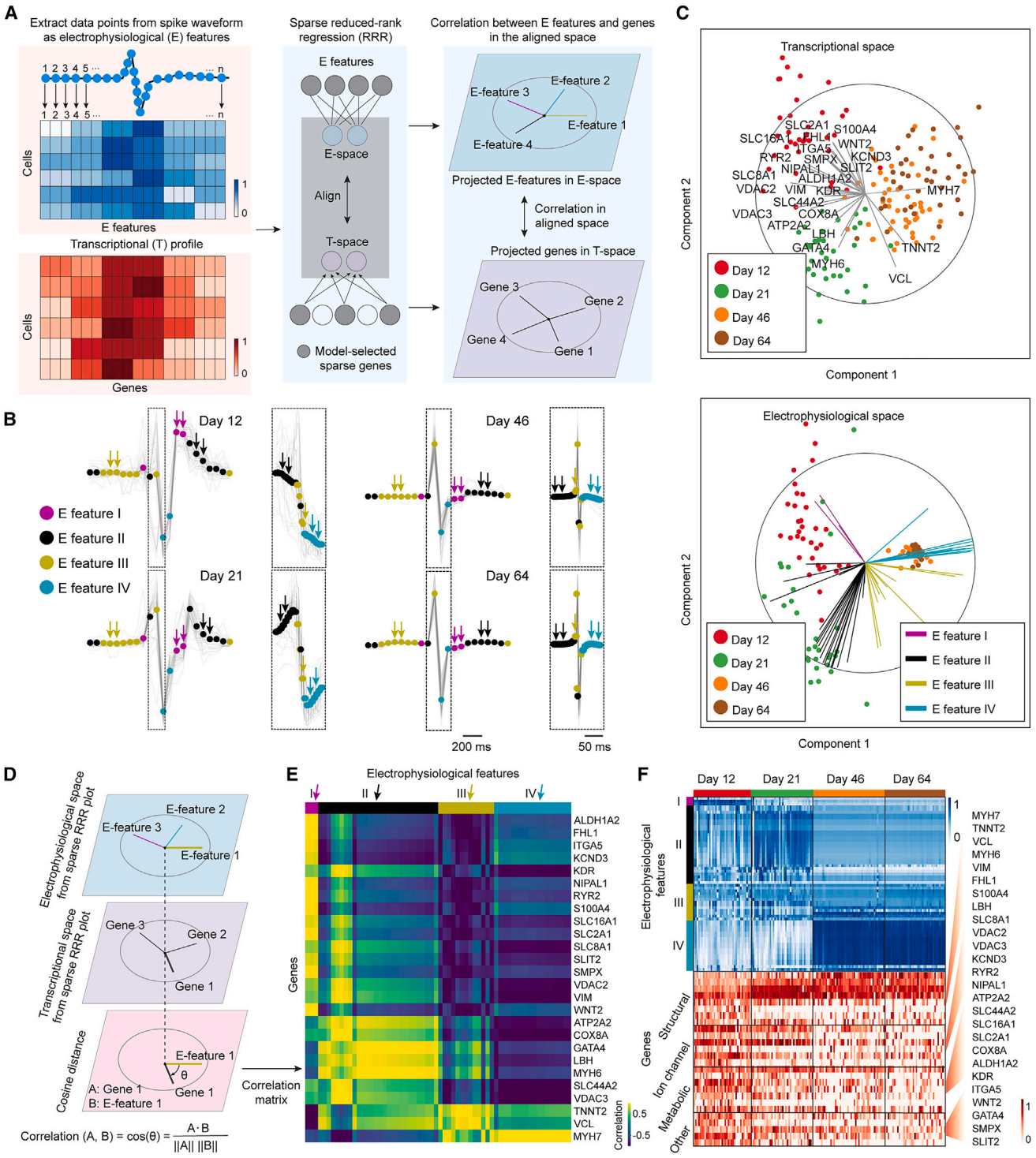

Figure 6. *In situ* electro-seq enables cross-modal visualization and correlation

(A) Schematics illustrating the overview of sparse reduced-rank regression (RRR) analysis for paired electrophysiological and transcriptional measurements.

(B) Representative electrophysiological (E) features extracted from each spike. 1.6-s waveforms are sampled in 22 bins. Inset shows 0.15-s fast spikes sampled in 40 bins.

(C) Sparse RRR model that visualizes and aligns transcriptional states and electrophysiological states of cells (see STAR Methods).

(D) Schematics showing the calculation of cosine distance between E features and genes from the sparse RRR model in (C).

(E) Heatmap showing the correlation calculated by cosine distance between E features and genes from the sparse RRR model in (C).

(F) Heatmap showing the normalized extracted E features and expressions of the sparse RRR model-selected genes.

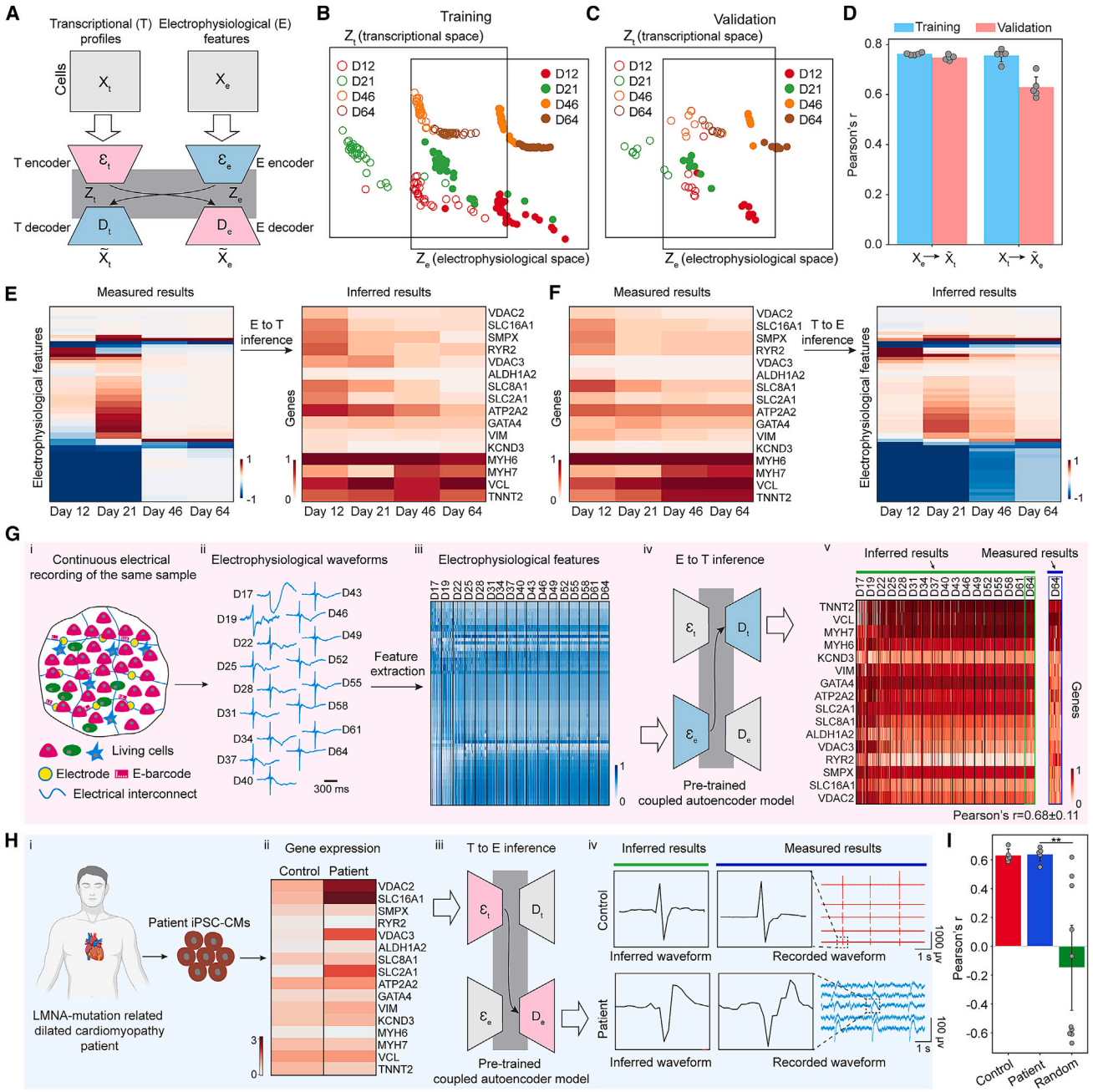

Figure 7. Machine-learning-based cross-modal inference

(A) Schematic showing the structure of a coupled autoencoder for electrophysiology-to-transcript (E-to-T) and transcript-to-electrophysiology (T-to-E) inference.

(B and C) Coupled autoencoder-encoded low-dimensional representations of the training data of *in situ* electro-seq samples at days 12, 21, 46, and 64 (B) and of the validation data split from days 12, 21, 46, and 64 data (C).

(D) Statistical summary of the performance of cross-modality ($Xt \rightarrow \bar{X}e$ *or* $Xe \rightarrow \bar{X}t$) inference. Error bars show mean ± SD over 5-fold cross-validation.

(E) Heatmap of normalized gene expression inferred from electrophysiological features.

(F) Heatmap of normalized electrophysiological features inferred from gene expression.

(G) Application of the pre-trained coupled autoencoder model to infer temporal dynamics of gene expression from the long-term recording of electrophysiological activity. (i) Schematics showing the long-term recording of electrophysiological activity. (ii) Electrophysiological waveforms measured from the sample. (iii) Heatmap showing normalized single-cell electrophysiological features. (iv) E-to-T inference. (v) Heatmap showing normalized single-cell gene expression profiles inferred by the coupled autoencoder (left panel) and measured results of gene expression (right panel).

(H) Application of the pre-trained coupled autoencoder model to infer the electrophysiology of patient-derived iPSC-CMs. (i) Schematic showing iPSC-CMs generated from a patient with LMNA-mutation-related DCM. (ii) Representative normalized gene expression profiles of LMNA-mutant and healthy hiPSC-CMs. (iii)

(legend continued on next page)

acknowledge that neighboring CMs coalesce through gap junctions and adhesive junctions to form the myocardium during development[43,44] and that hiPSC-CMs show a progressively organized ultrastructure during development.[4,43,45] As a result, extracellular electrical recordings could also reflect the activities of hiPSC-CM groups surrounding the electrode. We then tested an alternative computational pipeline by identifying all the cells surrounding the electrode for a multi-cell data analysis (Figure S6A). The multi-cell analysis recapitulates the same hiPSC-CM developmental trajectory, cell clustering, and electrophysiology-to-gene correlations (Figures S6 and S7) as the single-cell analysis, suggesting that single- and multi-cellular-level analysis may lead to consistent results when analyzing hiPSC-CM patches with relatively homogeneous cell composition.[43,45] The ability to record the single-cell activity was also tested and supported by primary neuron culture with diverse cell types (Figures 3 and S4), where single-cell resolution is necessary to register single-neuron electrophysiological activities with molecular cell types and states.

Future work may address potential opportunities. For example, integrating different flexible electronics with intracellular electrodes[46] and multifunctional sensors and stimulators (e.g., electrical, mechanical, optical, chemical, etc.)[47] with *in situ* sequencing of different biomolecules (e.g., RNA or DNA) could open up unlimited access to different biological systems. Incorporating STARmap Plus (~2,700 genes panels)[48] into our current *in situ* electro-seq platform could also obtain more in-depth genetic information. Further scaling up the multiplexity of electrode arrays and increasing the electrode density in mesh electronics can increase the number and percentage of recorded cells per sample. Furthermore, integrating complementary metal-oxide-semiconductor multiplexing circuits could also substantially increase the number of cells that can be simultaneously measured.[49] Mesh nanoelectronics have already been used for the recording of electrical activity in 3D organoids[14] and behaving animals.[13,15,50] Further development of *in situ* electro-seq may map single-cell gene expression and functions in organoids and *in vivo* tissue samples[13,15,50] during both healthy and diseased states. For example, tissue-wide electrophysiological dysfunction can be correlated with cell-level gene expression variation in models of neuropsychiatric diseases[51,52] (e.g., autism spectrum disorder, bipolar disorders, etc.) and cardiac diseases[53] (e.g., atrial fibrillation, ventricular tachycardia, etc.).

Limitations of the study

It is also noteworthy that, although we have successfully conducted cross-modal correlation and inference (Figures 6 and 7), the resulting gene-to-electrophysiology relationship should be interpreted as correlation, not causality. Further genetic perturbation or molecular inhibition experiments are needed to fully establish the causal relationship and underlying mechanisms between genes and their functions. In particular, the electrophysiological patterns may lag behind the change of RNA expression profiles because extra time is needed for mRNA to be translated to proteins, for proteins to be transported to their functional loci, and for single cells to grow and form biological networks. In our study, we sampled cell electrophysiology every 3 days, whereas the mRNAs typically only last for a few hours inside cells. Thus, at such a temporal resolution of 3 days, the temporal profiles of RNA can be reliably correlated with the paired recorded cell electrophysiology. However, for biological systems with fast kinetics at the scale of hours (e.g., embryonic development, acute genetic perturbation), the molecular cell states defined by RNA may not reflect the functional cell states measured at the same time, and vice versa. Therefore, developments of computational methods and theoretical models with the spatiotemporal and mechanistic information from RNA to protein to function, and their incorporation in electro-seq analysis, will further advance our understanding of cellular dynamics and cell-state transition in biological cells, organoids, and tissues.

STAR★METHODS

Detailed methods are provided in the online version of this paper and include the following:

- KEY RESOURCES TABLE
- RESOURCE AVAILABILITY
  - Lead contact
  - Materials availability
  - Data and code availability
- EXPERIMENTAL MODEL AND SUBJECT DETAILS
  - Cell lines
  - Primary cells
- METHOD DETAILS
  - Fabrication of stretchable mesh electrode array
  - Connection of mesh electrode array with cable
  - Electrochemical measurements
  - Cell culture and cardiomyocytes differentiation
  - Calcium imaging
  - Integration of mesh electronics with cardiac and neural patches
  - Electrophysiological measurement
  - Immunostaining and imaging
  - *In situ* sequencing
  - Calcium imaging analysis
  - Sarcomere analysis
  - *In situ* sequencing analysis
  - Locating recorded hiPSC-CMs
  - hiPSC-CM electrophysiology data processing
  - Spike sorting
  - Locating recorded neurons

T-to-E inference of healthy and patient iPSC-CMs. (iv) Inferred results (left panel) and measured results (right panel) of healthy (top panel) and LMNA-mutant iPSC-CMs (bottom panel).

(l) Performance on the T-to-E inference using gene expression profiles from healthy and LMNA-mutant iPSC-CMs, and random shuffling of LMNA-mutant iPSC-CM gene expression profiles, measured in terms of Pearson's r. Error bars show mean ± SD, n = 5 or 10, ** $p < 0.01$, two-tailed, unpaired t test.

- Weighted Nearest Neighbor (WNN)
- Pseudotime analysis
- Sparse reduced-rank regression (RRR) model and bibiplot
- Coupled autoencoder model

- QUANTIFICATION AND STATISTICAL ANALYSIS

SUPPLEMENTAL INFORMATION

Supplemental information can be found online at https://doi.org/10.1016/j.cell.2023.03.023.

ACKNOWLEDGMENTS

We acknowledge the helpful discussions from Jane Salant. and the early assistance from all members of our labs. J.L. acknowledges the support of the startup fund from the School of Engineering and Applied Sciences, Harvard University; NIH/NIMH 1RF1MH123948; NIH/NIDDK 1DP1DK130673; NSF ECCS-2038603; Harvard Stem Cell Institute Collaborative Seed Grant SG-0124-20-00; Aramont Fund for Emerging Science Research; and the William F. Milton Fund. X.W. acknowledges the support of the Searle Scholars Program, Thomas D. and Virginia W. Cabot Professorship, and Edward Scolnick Professorship. Y.H. acknowledges the support of the James Mills Peirce Fellowship from the Graduate School of Arts and Sciences of Harvard University. H. Sheng acknowledges the support of Aramont Fund for Emerging Science Research. H. Shi acknowledges the support of Helen Hay Whitney Foundation Postdoctoral Fellowship. L.X. acknowledges the support of the American Heart Association 20CDA35260081. The schematics of the patient in Figure 7Hi were created using Biorender. The human iPSC line (LMNA line) was obtained from Joseph C. Wu, MD, PhD at the Stanford Cardiovascular Institute, funded by NIH 75N92020D00019.

AUTHOR CONTRIBUTIONS

J.L. and X.W. conceived the idea; Q.L. cultured cells; R.L. fabricated and characterized mesh electronics; Q.L. and R.L. performed electrical recording; Q.L. and Z.L. prepared samples for *in situ* sequencing; Z.L. and X.S. conducted *in situ* sequencing experiments; X.T., Z.L., Q.L., R.L., J.H., Y.H., H.Z., and W.T. analyzed data; all authors prepared figures and wrote the manuscript; J.L. and X.W. supervised the study.

DECLARATION OF INTERESTS

J.L. is a co-founder of Axoft, Inc. X.W. is a co-founder of Stellaromics, Inc. Patent application related to the work is filed by Broad Institute.

Received: July 20, 2022
Revised: September 21, 2022
Accepted: March 16, 2023
Published: April 19, 2023

REFERENCES

1. Cadwell, C.R., Palasantza, A., Jiang, X., Berens, P., Deng, Q., Yilmaz, M., Reimer, J., Shen, S., Bethge, M., Tolias, K.F., et al. (2016). Electrophysiological, transcriptomic and morphologic profiling of single neurons using Patch-seq. Nat. Biotechnol. *34*, 199–203. https://doi.org/10.1038/nbt.3445.
2. Callaway, E.M., Adkins, R.S., Aldridge, A.I., Allen, S., Ament, S.A., An, X., Armand, E., Ascoli, G.A., Bakken, T.E., and Bandrowski, A. (2021). A multimodal cell census and atlas of the mammalian primary motor cortex. Nature *598*, 86–102. https://doi.org/10.1038/s41586-021-03950-0.
3. Fuzik, J., Zeisel, A., Máté, Z., Calvigioni, D., Yanagawa, Y., Szabó, G., Linnarsson, S., and Harkany, T. (2016). Integration of electrophysiological recordings with single-cell RNA-seq data identifies neuronal subtypes. Nat. Biotechnol. *34*, 175–183. https://doi.org/10.1038/nbt.3443.
4. Gerbin, K.A., Grancharova, T., Donovan-Maiye, R.M., Hendershott, M.C., Anderson, H.G., Brown, J.M., Chen, J., Dinh, S.Q., Gehring, J.L., Johnson, G.R., et al. (2021). Cell states beyond transcriptomics: integrating structural organization and gene expression in hiPSC-derived cardiomyocytes. Cell Syst. *12*, 670–687.e10. https://doi.org/10.1016/j.cels.2021.05.001.
5. Xiang, Y., Tanaka, Y., Patterson, B., Kang, Y.J., Govindaiah, G., Roselaar, N., Cakir, B., Kim, K.Y., Lombroso, A.P., Hwang, S.M., et al. (2017). Fusion of regionally specified hPSC-derived organoids models human brain development and interneuron migration. Cell Stem Cell *21*, 383–398.e7. https://doi.org/10.1016/j.stem.2017.07.007.
6. Jun, J.J., Steinmetz, N.A., Siegle, J.H., Denman, D.J., Bauza, M., Barbarits, B., Lee, A.K., Anastassiou, C.A., Andrei, A., Aydın, Ç., et al. (2017). Fully integrated silicon probes for high-density recording of neural activity. Nature *551*, 232–236. https://doi.org/10.1038/nature24636.
7. Musk, E.; Neuralink (2019). An integrated brain-machine interface platform with thousands of channels. J. Med. Internet Res. *21*, e16194. https://doi.org/10.2196/16194.
8. Viventi, J., Kim, D.H., Moss, J.D., Kim, Y.S., Blanco, J.A., Annetta, N., Hicks, A., Xiao, J., Huang, Y., Callans, D.J., et al. (2010). A conformal, bio-interfaced class of silicon electronics for mapping cardiac electrophysiology. Sci. Transl. Med. *2*, 24ra22. https://www.science.org/doi/10.1126/scitranslmed.3000738.
9. Regev, A., Teichmann, S.A., Lander, E.S., Amit, I., Benoist, C., Birney, E., Bodenmiller, B., Campbell, P., Carninci, P., Clatworthy, M., et al. (2017). The human cell atlas. eLife *6*, e27041. https://doi.org/10.7554/eLife.27041.
10. Stuart, T., and Satija, R. (2019). Integrative single-cell analysis. Nat. Rev. Genet. *20*, 257–272. https://doi.org/10.1038/s41576-019-0093-7.
11. Tang, F., Barbacioru, C., Wang, Y., Nordman, E., Lee, C., Xu, N., Wang, X., Bodeau, J., Tuch, B.B., Siddiqui, A., et al. (2009). mRNA-seq whole-transcriptome analysis of a single cell. Nat. Methods *6*, 377–382. https://doi.org/10.1038/nmeth.1315.
12. Xu, S., Yang, H., Menon, V., Lemire, A.L., Wang, L., Henry, F.E., Turaga, S.C., and Sternson, S.M. (2020). Behavioral state coding by molecularly defined paraventricular hypothalamic cell type ensembles. Science *370*, eabb2429. https://doi.org/10.1126/science.abb2494.
13. Fu, T.M., Hong, G., Zhou, T., Schuhmann, T.G., Viveros, R.D., and Lieber, C.M. (2016). Stable long-term chronic brain mapping at the single-neuron level. Nat. Methods *13*, 875–882. https://doi.org/10.1038/nmeth.3969.
14. Li, Q., Nan, K., Le Floch, P., Lin, Z., Sheng, H., Blum, T.S., and Liu, J. (2019). Cyborg organoids: implantation of nanoelectronics via organogenesis for tissue-wide electrophysiology. Nano Lett. *19*, 5781–5789. https://doi.org/10.1021/acs.nanolett.9b02512.
15. Liu, J., Fu, T.M., Cheng, Z., Hong, G., Zhou, T., Jin, L., Duvvuri, M., Jiang, Z., Kruskal, P., Xie, C., et al. (2015). Syringe-injectable electronics. Nat. Nanotechnol. *10*, 629–636. https://doi.org/10.1038/nnano.2015.115.
16. Liu, J., Xie, C., Dai, X., Jin, L., Zhou, W., and Lieber, C.M. (2013). Multifunctional three-dimensional macroporous nanoelectronic networks for smart materials. Proc. Natl. Acad. Sci. USA *110*, 6694–6699. https://doi.org/10.1073/pnas.1305209110.
17. Tian, B., Liu, J., Dvir, T., Jin, L., Tsui, J.H., Qing, Q., Suo, Z., Langer, R., Kohane, D.S., and Lieber, C.M. (2012). Macroporous nanowire nanoelectronic scaffolds for synthetic tissues. Nat. Mater. *11*, 986–994. https://doi.org/10.1038/nmat3404.
18. Wang, X., Allen, W.E., Wright, M.A., Sylwestrak, E.L., Samusik, N., Vesuna, S., Evans, K., Liu, C., Ramakrishnan, C., Liu, J., et al. (2018). Three-dimensional intact-tissue sequencing of single-cell transcriptional states. Science *361*, eaat5691. https://doi.org/10.1126/science.aat5691.
19. Feiner, R., Engel, L., Fleischer, S., Malki, M., Gal, I., Shapira, A., Shacham-Diamand, Y., and Dvir, T. (2016). Engineered hybrid cardiac patches with

multifunctional electronics for online monitoring and regulation of tissue function. Nat. Mater. *15*, 679–685. https://doi.org/10.1038/nmat4590.

20. Henze, D.A., Borhegyi, Z., Csicsvari, J., Mamiya, A., Harris, K.D., and Buzsáki, G. (2000). Intracellular features predicted by extracellular recordings in the hippocampus in vivo. J. Neurophysiol. *84*, 390–400. https://doi.org/10.1152/jn.2000.84.1.390.

21. Spira, M.E., and Hai, A. (2013). Multi-electrode array technologies for neuroscience and cardiology. Nat. Nanotechnol. *8*, 83–94. https://doi.org/10.1038/nnano.2012.265.

22. Steinmetz, N.A., Aydin, C., Lebedeva, A., Okun, M., Pachitariu, M., Bauza, M., Beau, M., Bhagat, J., Böhm, C., Broux, M., et al. (2021). Neuropixels 2.0: a miniaturized high-density probe for stable, long-term brain recordings. Science *372*, eabf4588. https://doi.org/10.1126/science.abf4588.

23. Hwang, H.S., Kryshtal, D.O., Feaster, T.K., Sánchez-Freire, V., Zhang, J., Kamp, T.J., Hong, C.C., Wu, J.C., and Knollmann, B.C. (2015). Comparable calcium handling of human iPSC-derived cardiomyocytes generated by multiple laboratories. J. Mol. Cell. Cardiol. *85*, 79–88. https://doi.org/10.1016/j.yjmcc.2015.05.003.

24. Churko, J.M., Garg, P., Treutlein, B., Venkatasubramanian, M., Wu, H., Lee, J., Wessells, Q.N., Chen, S.Y., Chen, W.Y., Chetal, K., et al. (2018). Defining human cardiac transcription factor hierarchies using integrated single-cell heterogeneity analysis. Nat. Commun. *9*, 4906. https://doi.org/10.1038/s41467-018-07333-4.

25. Cui, Y., Zheng, Y., Liu, X., Yan, L., Fan, X., Yong, J., Hu, Y., Dong, J., Li, Q., Wu, X., et al. (2019). Single-cell transcriptome analysis maps the developmental track of the human heart. Cell Rep. *26*, 1934–1950.e5. https://doi.org/10.1016/j.celrep.2019.01.079.

26. Friedman, C.E., Nguyen, Q., Lukowski, S.W., Helfer, A., Chiu, H.S., Miklas, J., Levy, S., Suo, S., Han, J.J., Osteil, P., et al. (2018). Single-cell transcriptomic analysis of cardiac differentiation from human PSCs reveals HOPX-dependent cardiomyocyte maturation. Cell Stem Cell *23*. 586.e8–598.e8. https://doi.org/10.1016/j.stem.2018.09.009.

27. Ruan, H., Liao, Y., Ren, Z., Mao, L., Yao, F., Yu, P., Ye, Y., Zhang, Z., Li, S., Xu, H., et al. (2019). Single-cell reconstruction of differentiation trajectory reveals a critical role of ETS1 in human cardiac lineage commitment. BMC Biol. *17*, 89. https://doi.org/10.1186/s12915-019-0709-6.

28. McInnes, L., Healy, J., Saul, N., and Großberger, L. (2018). UMAP: uniform manifold approximation and projection. J. Open Source Softw. *3*, 861. https://doi.org/10.21105/joss.00861.

29. He, Y., Tang, X., Huang, J., Ren, J., Zhou, H., Chen, K., Liu, A., Shi, H., Lin, Z., Li, Q., et al. (2021). ClusterMap for multi-scale clustering analysis of spatial gene expression. Nat. Commun. *12*, 5909. https://doi.org/10.1038/s41467-021-26044-x.

30. Traag, V.A., Waltman, L., and van Eck, N.J. (2019). From Louvain to Leiden: guaranteeing well-connected communities. Sci. Rep. *9*, 5233. https://doi.org/10.1038/s41598-019-41695-z.

31. Schoonover, C.E., Ohashi, S.N., Axel, R., and Fink, A.J.P. (2021). Representational drift in primary olfactory cortex. Nature *594*, 541–546. https://doi.org/10.1038/s41586-021-03628-7.

32. Li, L.Y., Xiong, X.R., Ibrahim, L.A., Yuan, W., Tao, H.W., and Zhang, L.I. (2015). Differential receptive field properties of parvalbumin and somatostatin inhibitory neurons in mouse auditory cortex. Cereb. Cortex *25*, 1782–1791. https://doi.org/10.1093/cercor/bht417.

33. Jia, X., Siegle, J.H., Bennett, C., Gale, S.D., Denman, D.J., Koch, C., and Olsen, S.R. (2019). High-density extracellular probes reveal dendritic backpropagation and facilitate neuron classification. J. Neurophysiol. *121*, 1831–1847. https://doi.org/10.1152/jn.00680.2018.

34. Lian, X., Hsiao, C., Wilson, G., Zhu, K., Hazeltine, L.B., Azarin, S.M., Raval, K.K., Zhang, J., Kamp, T.J., and Palecek, S.P. (2012). Robust cardiomyocyte differentiation from human pluripotent stem cells via temporal modulation of canonical Wnt signaling. Proc. Natl. Acad. Sci. USA *109*, E1848–E1857. https://doi.org/10.1073/pnas.1200250109.

35. Scala, F., Kobak, D., Bernabucci, M., Bernaerts, Y., Cadwell, C.R., Castro, J.R., Hartmanis, L., Jiang, X., Laturnus, S., Miranda, E., et al. (2021). Phenotypic variation of transcriptomic cell types in mouse motor cortex. Nature *598*, 144–150. https://doi.org/10.1038/s41586-020-2907-3.

36. Hao, Y., Hao, S., Andersen-Nissen, E., Mauck, W.M., Zheng, S., Butler, A., Lee, M.J., Wilk, A.J., Darby, C., Zager, M., et al. (2021). Integrated analysis of multimodal single-cell data. Cell *184*. 3573.e29–3587.e29. https://doi.org/10.1016/j.cell.2021.04.048.

37. Cao, J., Spielmann, M., Qiu, X., Huang, X., Ibrahim, D.M., Hill, A.J., Zhang, F., Mundlos, S., Christiansen, L., Steemers, F.J., et al. (2019). The single-cell transcriptional landscape of mammalian organogenesis. Nature *566*, 496–502. https://doi.org/10.1038/s41586-019-0969-x.

38. Kobak, D., Bernaerts, Y., Weis, M.A., Scala, F., Tolias, A.S., and Berens, P. (2021). Sparse reduced-rank regression for exploratory visualization of paired multivariate data. J. R. Stat. Soc. C *70*, 980–1000. https://doi.org/10.1111/rssc.12494.

39. Gala, R., Budzillo, A., Baftizadeh, F., Miller, J., Gouwens, N., Arkhipov, A., Murphy, G., Tasic, B., Zeng, H., Hawrylycz, M., and Sümbül, U. (2021). Consistent cross-modal identification of cortical neurons with coupled autoencoders. Nat. Comput. Sci. *1*, 120–127. https://doi.org/10.1038/s43588-021-00030-1.

40. Gala, R., Gouwens, N., Yao, Z., Budzillo, A., Penn, O., Tasic, B., Murphy, G., Zeng, H., and Sümbül, U. (2019). A coupled autoencoder approach for multi-modal analysis of cell types. https://arxiv.org/abs/1911.05663.

41. Gouwens, N.W., Sorensen, S.A., Baftizadeh, F., Budzillo, A., Lee, B.R., Jarsky, T., Alfiler, L., Baker, K., Barkan, E., Berry, K., et al. (2020). Integrated morphoelectric and transcriptomic classification of cortical GABAergic cells. Cell *183*, 935–953.e19. https://doi.org/10.1016/j.cell.2020.09.057.

42. Lee, J., Termglinchan, V., Diecke, S., Itzhaki, I., Lam, C.K., Garg, P., Lau, E., Greenhaw, M., Seeger, T., Wu, H., et al. (2019). Activation of PDGF pathway links LMNA mutation to dilated cardiomyopathy. Nature *572*, 335–340. https://doi.org/10.1038/s41586-019-1406-x.

43. Karbassi, E., Fenix, A., Marchiano, S., Muraoka, N., Nakamura, K., Yang, X., and Murry, C.E. (2020). Cardiomyocyte maturation: advances in knowledge and implications for regenerative medicine. Nat. Rev. Cardiol. *17*, 341–359. https://doi.org/10.1038/s41569-019-0331-x.

44. Laflamme, M.A., and Murry, C.E. (2011). Heart regeneration. Nature *473*, 326–335. https://doi.org/10.1038/nature10147.

45. Ronaldson-Bouchard, K., Ma, S.P., Yeager, K., Chen, T., Song, L., Sirabella, D., Morikawa, K., Teles, D., Yazawa, M., and Vunjak-Novakovic, G. (2018). Advanced maturation of human cardiac tissue grown from pluripotent stem cells. Nature *556*, 239–243. https://doi.org/10.1038/s41586-018-0016-3.

46. Abbott, J., Ye, T., Krenek, K., Gertner, R.S., Ban, S., Kim, Y., Qin, L., Wu, W., Park, H., and Ham, D. (2020). A nanoelectrode array for obtaining intracellular recordings from thousands of connected neurons. Nat. Biomed. Eng. *4*, 232–241. https://doi.org/10.1038/s41551-019-0455-7.

47. Rogers, J.A., Ghaffari, R., and Kim, D.-H. (2016). Stretchable Bioelectronics for Medical Devices and Systems (Springer).

48. Zeng, H., Huang, J., Zhou, H., Meilandt, W.J., Dejanovic, B., Zhou, Y., Bohlen, C.J., Lee, S.-H., Ren, J., Liu, A., et al. (2022). Integrative in situ mapping of single-cell transcriptional states and tissue histopathology in an Alzheimer's disease model. Nat. Neurosci. *26*, 430–446. https://doi.org/10.1038/s41593-022-01251-x.

49. Viventi, J., Kim, D.H., Vigeland, L., Frechette, E.S., Blanco, J.A., Kim, Y.S., Avrin, A.E., Tiruvadi, V.R., Hwang, S.W., Vanleer, A.C., et al. (2011). Flexible, foldable, actively multiplexed, high-density electrode array for mapping brain activity in vivo. Nat. Neurosci. *14*, 1599–1605. https://doi.org/10.1038/nn.2973.

50. Zhao, S., Tang, X., Tian, W., Partarrieu, S., Liu, R., Shen, H., Lee, J., Guo, S., Lin, Z., and Liu, J. (2023). Tracking neural activity from the same cells

during the entire adult life of mice. Nat. Neurosci. https://doi.org/10.1038/s41593-023-01267-x.

51. Quadrato, G., Brown, J., and Arlotta, P. (2016). The promises and challenges of human brain organoids as models of neuropsychiatric disease. Nat. Med. *22*, 1220–1228. https://doi.org/10.1038/nm.4214.
52. Sanders, S.J., Sahin, M., Hostyk, J., Thurm, A., Jacquemont, S., Avillach, P., Douard, E., Martin, C.L., Modi, M.E., Moreno-De-Luca, A., et al. (2019). A framework for the investigation of rare genetic disorders in neuropsychiatry. Nat. Med. *25*, 1477–1487. https://doi.org/10.1038/s41591-019-0581-5.
53. Liu, J., Zhang, X., Liu, Y., Rodrigo, M., Loftus, P.D., Aparicio-Valenzuela, J., Zheng, J., Pong, T., Cyr, K.J., Babakhanian, M., et al. (2020). Intrinsically stretchable electrode array enabled in vivo electrophysiological mapping of atrial fibrillation at cellular resolution. Proc. Natl. Acad. Sci. USA *117*, 14769–14778. https://doi.org/10.1073/pnas.2000207117.
54. Wolf, F.A., Angerer, P., and Theis, F.J. (2018). SCANPY: large-scale single-cell gene expression data analysis. Genome Biol. *19*, 15. https://doi.org/10.1186/s13059-017-1382-0.
55. Johnson, W.E., Li, C., and Rabinovic, A. (2007). Adjusting batch effects in microarray expression data using empirical Bayes methods. Biostatistics *8*, 118–127. https://doi.org/10.1093/biostatistics/kxj037.
56. Lee, G., Gommers, R., Waselewski, F., Wohlfahrt, K., and O'Leary, A. (2019). PyWavelets: a Python package for wavelet analysis. J. Open Source Softw. *4*, 1237. https://doi.org/10.21105/joss.01237.
57. Chung, J.E., Magland, J.F., Barnett, A.H., Tolosa, V.M., Tooker, A.C., Lee, K.Y., Shah, K.G., Felix, S.H., Frank, L.M., and Greengard, L.F. (2017). A fully automated approach to spike sorting. Neuron *95*, 1381–1394.e6. https://doi.org/10.1016/j.neuron.2017.08.030.
58. Buccino, A.P., Hurwitz, C.L., Garcia, S., Magland, J., Siegle, J.H., Hurwitz, R., and Hennig, M.H. (2020). SpikeInterface, a unified framework for spike sorting. eLife *9*, e61834. https://doi.org/10.7554/eLife.61834.
59. Bradski, G. (2000). The openCV library. Dr. Dobb's J. Softw. Tool. Prof. Program. *25*, 120–123.
60. Lin, Z., Garbern, J.C., Liu, R., Li, Q., Mancheño Juncosa, E., Elwell, H.L., Sokol, M., Aoyama, J., Deumer, U.S., Hsiao, E., et al. (2023). Tissue-embedded stretchable nanoelectronics reveal endothelial cell–mediated electrical maturation of human 3D cardiac microtissues. Sci. Adv. *9*, eade8513. https://doi.org/10.1126/sciadv.ade8513.
61. Feltham, A.M., and Spiro, M. (1971). Platinized platinum electrodes. Chem. Rev. *71*, 177–193. https://doi.org/10.1021/cr60270a002.
62. Lian, X., Zhang, J., Azarin, S.M., Zhu, K., Hazeltine, L.B., Bao, X., Hsiao, C., Kamp, T.J., and Palecek, S.P. (2013). Directed cardiomyocyte differentiation from human pluripotent stem cells by modulating Wnt/beta-catenin signaling under fully defined conditions. Nat. Protoc. *8*, 162–175. https://doi.org/10.1038/nprot.2012.150.
63. Timko, B.P., Cohen-Karni, T., Yu, G., Qing, Q., Tian, B., and Lieber, C.M. (2009). Electrical recording from hearts with flexible nanowire device arrays. Nano Lett. *9*, 914–918. https://doi.org/10.1021/nl900096z.
64. Sutcliffe, M.D., Tan, P.M., Fernandez-Perez, A., Nam, Y.J., Munshi, N.V., and Saucerman, J.J. (2018). High content analysis identifies unique morphological features of reprogrammed cardiomyocytes. Sci. Rep. *8*, 1258. https://doi.org/10.1038/s41598-018-19539-z.

STAR★METHODS

KEY RESOURCES TABLE

REAGENT or RESOURCE	SOURCE	IDENTIFIER
Antibodies		
Rabbit polyclonal anti-HCN4 antibody	Sigma-Aldrich	Cat#AB5808; RRID: AB_11214197
Mouse monoclonal anti-MYH6 antibody	Sigma-Aldrich	Cat#AMAB90950; RRID: AB_2665730
Mouse cardiac troponin T monoclonal antibody (13-11)	Invitrogen	Cat#MA5-12960; RRID: AB_11000742
Mouse monoclonal anti-alpha-actinin antibody	Sigma-Aldrich	Cat#A7811; RRID: AB_476766
Alexa Fluor 594 AffiniPure Donkey Anti-Mouse IgG (H+L)	Jackson Immuno Research Labs	Cat#NC0322938; RRID: AB_2340854
Alexa Fluor™ Plus 647 Donkey anti-Mouse IgG (H+L)	Invitrogen	Cat#A32787; RRID: AB_2762830
Alexa Fluor™ 594 Donkey anti-Rabbit IgG (H+L)	Invitrogen	Cat#A-21207; RRID: AB_141637
Biological samples		
Mouse primary hippocampal neurons	Broad Institute of MIT and Harvard	C57BL/6 mice
Chemicals, peptides, and recombinant proteins		
4',6-diamidino-2-phenylindole (DAPI)	Sigma-Aldrich	Cat#D9542
Rhodamine 6G powder	Sigma-Aldrich	Cat#989-38-8
Chloroplatinic acid (H_2PtCl_6) solution	Sigma-Aldrich	Cat#16941-12-1
Essential 8 medium	Gibco Life Technologies	Cat#A1517001
RPMI 1640 medium	Gibco Life Technologies	Cat#11875093
B27-insulin supplement	Gibco Life Technologies	Cat#A1895601
CHIR99021	BioVision	Cat#1677; CAS: 252917-06-9
IWR1	Cayman Chemical Company	13659; CAS: 1127442-82-3
B27 supplement	Gibco Life Technologies	Cat#17504044
NbActiv4 (NB4)	BrainBits	Cat# NB4
Oregon Green®488 BAPTA-1	Invitrogen	Cat# O6807
Poly-D-lysine	Sigma-Aldrich	Cat# P7280-5X5MG
Matrigel	Corning	Cat# 08-774-552
Trypsin-EDTA	Gibco Life Technologies	Cat# 25200056
Trypan blue solution, 0.4%	Gibco Life Technologies	Cat# 15-250-061
Rock inhibitor (Y27632)	Tocris Bioscience	Cat# 12-541-0
Blebblistatin	Sigma-Aldrich	Cat# 856925-71-8
Norepinephrine	Sigma-Aldrich	Cat# 48-935-0100MG
Glass-bottom 12-well plates	Mattek	Cat# P12G-1.5-14-F
Gel slick solution	Lonza	Cat# 50640
PlusOne bind-silane	GE Healthcare	Cat# 17-1330-01
Acetic acid	Sigma-Aldrich	Cat# A6283-100ML
Circular cover glass	Electron Microscope Sciences	Cat# 72226-01
16% PFA, EM grade	Electron Microscope Sciences	Cat# 15710-S
Triton-X-100, 10% solution	Sigma-Aldrich	Cat# 93443
OminiPur formamide	Calbiochem	Cat# 4610-OP
OmniPur SDS, 20%	Calbiochem	Cat# 7990-OP
20×SSC buffer	Sigma-Aldrich	Cat# S6639
Glycine	Sigma-Aldrich	Cat# 50046-250G
Ribonucleoside vanadyl complex	New England Biolabs	Cat# S1402S
Proteinase K Solution (20 mg/mL), RNA grade	Invitrogen	Cat# 25530049
Yeast tRNA (10 mg/mL)	Thermo Fisher Scientific	Cat# AM7119
SUPERase·In RNase Inhibitor	Invitrogen	Cat# AM2696

(*Continued on next page*)

Continued

REAGENT or RESOURCE	SOURCE	IDENTIFIER
T4 DNA ligase	Thermo Fisher Scientific	Cat# EL0011
Phi29 DNA polymerase	Thermo Fisher Scientific	Cat# EP0094
dNTP mix	Invitrogen	Cat# 100004893
BSA, molecular biology grade	New England Biolabs	Cat# B9000S
5-(3-aminoallyl)-dUTP	Invitrogen	Cat# AM8439
Methacrylic acid N-hydroxysuccinimide ester, 98%	Sigma-Aldrich	Cat# 730300-1G
DMSO, anhydrous	Thermo Fisher Scientific	Cat# D12345
Acrylamide solution, 40%	Bio-Rad	Cat# 161-0140
Bis solution, 2%	Bio-Rad	Cat# 161-0142
Ammonium persulfate	Sigma-Aldrich	Cat# A3678
N,N,N′,N′-Tetramethylethylenediamine	Sigma-Aldrich	Cat# T9281
Antarctic phosphatase	New England Biolabs	Cat# M0289L
10×PBS, pH7.4	Thermo Scientific	Cat# 70011044
1×PBS, pH7.4	Thermo Fisher Scientific	Cat# 10010049
Ethanol	VWR	Cat# 89125-170
DNase/RNase-Free Distilled Water	Thermo Fisher Scientific	Cat# 10977023
Experimental models: Cell lines		
Human induced pluripotent stem cells	WiCell Research Institute	hiPSC-IMR90-1
Oligonucleotides		
Probe sequences for cardiac tissue	IDT	See Table S1
Probe sequences for neuron tissue	IDT	See Table S2
Deposited data and code		
In situ sequencing data	Single Cell Portal	https://singlecell.broadinstitute.org/single_cell/study/SCP1346
Multimodal data and Code	Github	https://github.com/LiuLab-Bioelectronics-Harvard/electro-seq
Software and algorithms		
MATLAB	MathWorks	https://www.mathworks.com/products/matlab.html
R	R Core	https://www.r-project.org/
Python	Python Software Foundation	https://www.python.org/
Monocle 3	Cao et al.[37]	https://github.com/cole-trapnell-lab/monocle3
Uniform manifold approximation and projection (UMAP)	McInnes et al.[28]	https://github.com/lmcinnes/umap
ClusterMap	He et al.[29]	https://github.com/wanglab-broad/ClusterMap
Scanpy v1.6.0	Wolf et al.[54]	https://scanpy.readthedocs.io/en/stable/
Combat	Johnson et al.[55]	http://www.bioconductor.org/packages/release/bioc/html/sva.html
Leiden clustering	Traag et al.[30]	https://github.com/vtraag/leidenalg
PyWavelets v1.1.0	Lee et al.[56]	https://github.com/PyWavelets/pywt/blob/master/doc/release/1.1.0-notes.rst
Seurat v4	Hao et al.[36]	https://satijalab.org/seurat/
Sparse reduced-rank regression (RRR)	Kobak et al.[38]	https://github.com/berenslab/patch-seq-rrr
Coupled autoencoder	Gala et al.[39]	https://github.com/AllenInstitute/coupledAE-patchseq
MountainSort	Chung et al.[57]	https://github.com/flatironinstitute/mountainsort

(*Continued on next page*)

Continued

REAGENT or RESOURCE	SOURCE	IDENTIFIER
SpikeInterface v0.9	Buccino et al.[58]	https://github.com/SpikeInterface
Fiji	Image J	https://imagej.net/software/fiji/
ChimeraX	ChimeraX	https://www.cgl.ucsf.edu/chimerax/
Blackroch Python-Utilities	Blackroch Neurotech	https://github.com/Blackrock Neurotech/Python-Utilities
Blackrock research central software suite 7.04	Blackroch Neurotech	https://blackrockneurotech.com/
Opencv-python v4.5.5.64	Bradski[59]	https://github.com/opencv/opencv-python
Biorender	Biorender	https://biorender.com/

RESOURCE AVAILABILITY

Lead contact

Further information and requests for reagents and resources should be directed to and will be fulfilled by the Lead Contact, Jia Liu (jia_liu@seas.harvard.edu).

Materials availability

This study did not generate new reagents.

Data and code availability

- All the *in situ* sequencing data are available in the Single Cell Portal at https://singlecell.broadinstitute.org/single_cell/study/SCP1346 and are publicly available as of the date of publication. Microscopy data reported in this paper will be shared by the lead contact upon request.
- All the code are available in the GitHub repository at https://github.com/LiuLab-Bioelectronics-Harvard/electro-seq and are publicly available as of the date of publication.
- Any additional information required to reanalyze the data reported in this paper is available from the lead contact upon request.

EXPERIMENTAL MODEL AND SUBJECT DETAILS

Cell lines

Human induced pluripotent stem cells (hiPSC, hiPSC-IMR90-1) were obtained from the WiCell Research Institute (Madison, WI, USA). Authentication and testing for the mycoplasma were performed by the WiCell Research Institute. The use of Cells (hiPSC, hiPSC-IMR90-1) was approved/provided by the University of Wisconsin, agreement number 19-WO280. The human iPSC line (LMNA line) was obtained from Joseph C. Wu, MD, PhD at the Stanford Cardiovascular Institute. hiPSC and hiPSC-derived cardiomyocytes (CMs) were cultured at 37°C and 5% CO_2 in Essential 8 medium (Gibco) and RPMI 1640 medium (Gibco) plus 1% B27 supplement (Gibco), respectively.

Primary cells

Primary hippocampal neurons were obtained from the Broad Institute of MIT and Harvard. The neurons were maintained at 37°C and 5% CO_2 in NbActiv4 (NB4, BrainBits) medium.

METHOD DETAILS

Fabrication of stretchable mesh electrode array

Fabrication of the ultra-flexible, stretchable mesh nanoelectronics was based on methods described previously.[14,15,17,60] Key steps are described as follows: 4-inch glass wafers (Soda lime glass) were used as a transparent and insulating substrate for fabrication and cell culture. The glass wafers were cleaned with piranha solution (3:1 mixture of sulfuric acid and 30% hydrogen peroxide), followed by rinsing with deionized (DI) water and drying with the N_2. Hexamethyldisilazane (HMDS, MicroChem) was spin-coated at 4000 rpm to increase the adhesion of photoresists with the substrate. LOR 3A (300 nm, MicroChem)/S1805 (500 nm, MicroChem) were spin-coated at 4000 rpm/4000 rpm, followed by baking at 180°C for 5 mins and at 115 °C for 1 min, respectively. Ni sacrificial layer was exposed by using a Karl Suss MA6 mask aligner with 365 nm ultraviolet (UV) light at 40 mJ/cm^2 and developed by CD-26 developer (MICROPOSIT) for 70 s. O_2 plasma (Anatech Barrel Plasma System) was used for the removal of photoresist residues at 50 W for 30 s.

Sharon Thermal Evaporator was used for the deposition of 100-nm-thick Ni followed by a standard lift-off procedure in remover PG (MicroChem) for 2 hours. After patterning the Ni layer, SU-8 precursor (SU-8 2000.5, MicroChem) was spin-coated at 4000 rpm, pre-baked at 65°C / 95°C for 2 mins each, exposed to 365 nm UV at 200 mJ/cm^2, post-baked at 65°C / 95°C for 2 mins each, developed using SU-8 developer (MicroChem) for 60 s, rinsed by isopropyl alcohol (IPA) for 30 s, blow for drying by N_2 gun, and hard-baked at 180°C for 40 mins to define mesh-like SU-8 400-nm-thick patterns as the bottom encapsulation layer. After patterning the SU-8 bottom layer, HMDS/LOR3A/S1805 photoresist layers were spin-coated as described above, followed by depositing 5/40/5-nm-thick chromium/gold/chromium (Cr/Au/Cr) by the electron-beam evaporator (Denton), and the standard lift-off procedure in the remover PG (MicroChem) overnight to define the Cr/Au/Cr interconnects. Then, the same photolithography process was used to define 5/50-nm-thick chromium/platinum (Cr/Pt) as electrodes. After patterning electrodes, the top SU-8 encapsulating layer was patterned using the same method described for patterning the bottom SU-8 layer. Finally, fluorescent E-barcodes were defined by patterning the SU-8 structure doped by adding 0.004 wt‰ of Rhodamine 6G powder (Sigma-Aldrich) into the SU-8 precursor.

Connection of mesh electrode array with cable

Next, the flexible flat cable (FFC, Molex) was soldered onto the input/output pads using a flip-chip bonder (Finetech Fineplacer), followed by gluing a culture chamber onto the substrate wafer to completely enclose the mesh part of the device using a biocompatible adhesive (Kwik-Sil, WPI). Then, Pt black (PtB) was electroplated on the Pt electrode array using a precursor of 0.08 wt% chloroplatinic acid (H_2PtCl_6) solution (Sigma-Aldrich) in H_2O. The precursor was drop-casted onto the device, followed by passage of a 1 mA/cm^2 DC electric current density for 3 mins using mesh electrodes as anodes and an external Pt wire as the cathode. The device was then rinsed with DI water for 30 s and dried by N_2. Finally, the surface of the device was treated with oxygen plasma (Anatech 106 oxygen plasma barrel asher), followed by adding 1 mL of Ni etchant (type TFB, Transene) into the chamber for 2 to 4 hours to completely release the mesh electronics from the glass substrate. The device was then ready for subsequent sterilization steps before cell culture.

Electrochemical measurements

The electrochemical impedance spectra (EIS) of the electrodes were measured based on methods described previously.[61] The three-electrodes setup was used to measure the EIS of each electrode. A standard silver/silver chloride (Ag/AgCl) electrode and platinum wire (300 μm in diameter, 1.5 cm in length immersed) were used as reference electrode and counter electrode, respectively. The device was immersed in 1 X PBS solution (Thermofisher) during measurement. The SP-150 potentiostat (Bio-logic), along with its commercial software EC-lab, was used to perform the measurements. For each measurement, at least three frequency sweeps were measured from 1 MHz down to 1 Hz to obtain statistical results. A sinusoidal voltage of 100 mV peak-to-peak was applied. For each data point, the response to 10 consecutive sinusoids (spaced out by 10% of the period duration) was accumulated and averaged.

Cell culture and cardiomyocytes differentiation

Human induced pluripotent stem cells (hiPSC, hiPSC-IMR90-1) were obtained from the WiCell Research Institute (Madison, WI, USA). Authentication and testing for the mycoplasma were performed by the WiCell Research Institute. The human iPSC line (LMNA line) was obtained from Joseph C. Wu, MD, PhD at the Stanford Cardiovascular Institute. hiPSC cells were cultured on a Matrigel-coated 6-well plate with Essential 8 medium (Gibco). The medium was changed daily. The cells were passaged every 3-4 days. hiPSC-derived cardiomyocytes were generated according to the methods described previously with minor modification.[34,42,62] The hiPSC cells were cultured on a Matrigel-coated 6-well plate with Essential 8 medium to 70% - 80% confluency before initiating cardiac differentiation. The first day was defined as Day 0. For cardiac differentiation, the cells were maintained in RPMI 1640 medium (Gibco) plus 1% B27-insulin (Gibco). CHIR99021 (12 μM; BioVision) was applied on Day 0 for hiPSC-IMR90-1 cells while CHIR99021 (6 μM; BioVision) was applied on Day 0 to Day 1 for LMNA hiPSC cells according to the previous protocol;[42] IWR1 (5 μM; Cayman) was applied from Day 3 to Day 4. The cardiac cells were maintained in RPMI 1640 medium plus 1% B27 (Gibco) from Day 7, and the medium was changed every other day accordingly. Only the batches of hiPSC-CMs passed quality control - namely, showing clear beating on Day 8 of differentiation, were used for *in situ* electro-seq experiments. Primary hippocampal neurons were obtained from the Broad Institute of MIT and Harvard. The medium NbActiv4 (NB4, BrainBits) were used for the primary neuron cultures. All experiments involving human cells were approved by the Harvard University IRB and ESCRO committees.

Calcium imaging

For 2D cardiomyocyte calcium imaging, the cells at Day 9 of differentiation were dissociated into single cells and seeded onto the glass-bottom 12-well plate. On Day 12, Day 21, Day 46, and Day 64 of differentiation, 5 μM Oregon Green®488 BAPTA-1 (Invitrogen) was applied for 30 min and washed with DPBS. Then the cells were imaged using Leica TCS SP8 confocal microscope. For locating the electrical recorded cells, the cardiomyocytes were seeded onto the unreleased mesh electronics. After one week culture, 5 μM Oregon Green®488 BAPTA-1 (Invitrogen) was applied for 30 mins and washed with DPBS. Electrical signal was recorded and then the cells were imaged using Leica TCS SP8 confocal microscope.

Integration of mesh electronics with cardiac and neural patches

First, the released stretchable mesh electronics in the culture chamber was rinsed with DI water, decontaminated by 70% ethanol and incubated with Poly-D-lysine hydrobromide (0.01% w/v) overnight followed by coating with Matrigel solution (100 μg/mL) for about 1 hour at 37 °C. Then, the device was pre-chilled on an ice bag in the biosafety hood, and then 70 μL Matrigel solution (10 mg/mL) was added from the edge of the chamber, ensuring that the Matrigel covered the entire bottom substrate of the cell culture chamber underneath the stretchable mesh electronics. Next, the device was transferred into the incubator for at least 30 mins at 37°C to cure the Matrigel solution into a Matrigel hydrogel layer. Finally, hiPSC-CMs were incubated with 0.05% Trypsin-EDTA solution (Gibco) for 5 mins and then dissociated into single cells. Cell counting and viability were assessed by trypan blue (Gibco) staining method. 4 million cells (live cell percentage > 85%) were suspended in 1 mL RPMI 1640 medium plus 1% B27 and then transferred onto the cured electronics / Matrigel hybrids in the cell culture chamber and maintained at 37°C, 5% CO_2. 5 μM rock inhibitor (Y27632) was added to the medium in the first day to improve the cell viability. The CMs formed a continuous cell patch with the stretchable mesh electronics embedded within 24-48 hours. The cell culture medium was changed every other day. For neural patch integration, the primary hippocampal neurons were kindly obtained from the Broad Institute of MIT and Harvard. Single cells were seeded onto the mesh electronics. Cells were cultured in NbActiv4 medium (NB4, BrainBits). No medium changes were done in the first three days and then half were changed every other day afterwards.

Electrophysiological measurement

The Blackrock CerePlex Direct voltage amplifier along with a 32-channel Blackrock μ digital headstage connected to the device were used to record electrical activity from the samples. The culture medium was grounded by a Pt electrode. A second Pt electrode was used as a reference electrode. During electrical measurement, samples were placed on a battery powered warming plate that maintained thermostatic 37°C. The measurement setup was placed into a Faraday cage. A sampling rate of 10,000 Hz was used for the electrical recording. The cell electrical activities were recorded every 3 days. *MATLAB* and *Python* codes provided by Blackrock were used to load, view, and convert raw data files into an accessible format for data analysis. For drug tests,[17,63] the electrical signal was recorded, and then 100 μM blebblistatin (Sigma-Aldrich) or 1 μM norepinephrine (Fisher) was injected into the cell culture medium of the samples. The electrical signal before and after the drug application was recorded. Data analysis and statistical tests were performed by GraphPad Prism.

Immunostaining and imaging

Cells maintained on 2D surfaces were fixed with 4% paraformaldehyde (PFA) at room temperature for 15 mins, permeabilized with 0.25% Triton X-100 for 15 mins and blocked with 5% donkey serum for 1 hour. Cells were then incubated with primary antibodies (HCN4, AB5808, Sigma-Aldrich; MYH6, AMAB90950, Sigma-Aldrich; TNT, MA5-12960, Invitrogen; α-actinin, A7811, Sigma-Aldrich) at 4 °C overnight. After extensive washing, secondary antibodies were applied and incubated for another 2 hours at room temperature. Finally, 4',6-diamidino-2-phenylindole (DAPI, D9542, Sigma-Aldrich) was added and stained for 10 mins at room temperature. Cells were washed with PBS three times before imaging using Leica TCS SP8 confocal microscope. For cell-electronics hybrid staining, the samples were cleared and immunostained as previously described.[14] The primary antibodies were stained for 4 days, and the secondary antibodies were stained for 2 days, respectively. The samples were submerged in optical clearing solution overnight and embedded in 1% agarose gel before imaging using Leica TCS SP8 confocal microscope. Imaging was analyzed by *Fiji*.

In situ sequencing

Probes for cardiac and neural patches *in situ* sequencing were listed in Tables S1 and S2, respectively. *In situ* sequencing experiments were performed based on methods described previously with some modifications.[18] Briefly, the custom padlock probe and primer hybridize to mRNAs of the 3D cell-electronics hybrid, followed by enzymatic ligation and rolling circle amplification (RCA) to construct *in situ* cDNA amplicons. The amplicons are then copolymerized with acrylamide, forming a hydrogel network. A gene-specific identifier in the probe is amplified and decoded through multiple sequencing cycles (Figure 1G).

Glass-bottom 12-well plates (Mattek, P12G-1.5-14-F) were first treated with oxygen plasma for 5 mins (Anatech Barrel Plasma System, 100W, 40% O_2) followed by methacryloxypropyltrimethoxysilane (Bind-Silane) solution (88% ethanol, 10% acetic acid, 1% Bind-Silane, 1% H_2O) treatment for 1 hour. The 12-well plates were then rinsed with ethanol for 3 times and were left to dry at room temperature (R.T.) for 3 hours. The 12-well plates were further treated with 0.1 mg/mL of Poly-D-lysine solution for 1 hour at R.T. followed by 3 times rinsing with H_2O. The plates were air-dried for 1 hour at R.T. Micro cover glasses (12 mm) were pretreated with Gel Slick at R.T. for 10 mins and were then air-dried before using.

The cardiac or neural patch was fixed with 1 mL 1.6% PFA for 30 mins at R.T. and then washed with PBS 3 times for 10 mins each time. The sample was then transferred from the chamber to the 12-well plates and permeabilized with 1 mL (0.1 M glycine, 0.1 U/μL SUPERase·In, 0.5% Triton-X 100 in PBS) for 30 mins. The sample was washed with 1 mL PBST (0.1% Triton-X 100 in PBS) 3 times for 10 mins each. The sample was then incubated in 1X hybridization buffer (2X SSC, 10% formamide, 1% Triton-X 100, 20 mM RVC, 0.1 mg/mL yeast tRNA, 0.2% SDS and pooled SNAIL probes at 20 nM per oligo) in a 40 °C humidified oven with gentle shaking for 48 hours. The sample was washed with 1 mL PBSTV (1% RVC in PBST) at 37°C 3 times for 20 mins each and washed with high salt buffer (4X SSC in PBST) for another 20 mins at 37°C, and then washed with PBST three times for 10 mins each at R.T. The sample was then incubated in 1 mL ligation mixture (1:50 T4 DNA ligase, 1:100 BSA, 0.2 U/μL SUPERase·In) at R.T. overnight and then washed

with 1 mL PBST three times for 10 mins each. The sample was incubated in 1 mL RCA mixture (1:50 Phi29 DNA polymerase, 250 μM dNTP, 1:100 BSA, 0.2 U/μL SUPERase·In and 20 μM 5-(3-aminoallyl)-dUTP) at 4°C for 1 hour before incubating at 30°C for 6 hours and then washed with 1 mL PBST 3 times for 10 mins each. The sample was incubated with 20 mM methacrylic acid N-hydroxysuccinimide ester (dissolved in DMSO) in PBST for 3 hours at R.T. and washed with PBST 3 times for 10 mins each. The sample was then incubated with monomer buffer (4% acrylamide, 0.2% bis-acrylamide, 2X SSC) overnight at R.T. The buffer was then aspirated and 55 μL of polymerization mixture (0.2% ammonium persulfate, 0.2% tetramethylethylenediamine dissolved in monomer buffer) was added to the sample. The Gel Slick coated coverslip was immediately put on the sample and the polymerization was conducted in an N_2 container for 90 mins. The sample was then washed with PBST 3 times for 10 mins each.

Five cycles of sequencing experiments were performed to decode gene identity. Within each cycle, the sample was first treated with a stripping buffer (60% formamide, 0.1% Triton-X-100) at R.T. for 6 times, 15 mins each, followed by PBST wash for 6 times, 10 mins each. Then the sample was incubated with the sequencing mixture (1:25 T4 DNA ligase, 1:100 BSA, 10 μM reading probe, and 5 μM fluorescent oligos) at R.T. for 12 hours. Then the sample was washed by the washing and imaging buffer (2XSSC, 10% formamide and 0.1% Triton-X-100) for 5 times, 10 mins each. DAPI was dissolved in PBST and used for nuclei staining for 20 mins. Finally, the sample was immersed in the washing and imaging buffer for imaging. Image acquisition was performed with Leica TCS SP8 confocal microscope with 25X water-immersion objective (NA 0.95), with a voxel size around 230 nm X 230 nm X 570 nm.

Calcium imaging analysis

For hiPSC-CMs during development, the calcium image was first segmented using the watershed segmentation method; the calcium signal trace was then normalized for each segmented cell. The *findpeaks* function in *MATLAB(2019b)* was used to detect each calcium spike, and all detected spikes for the cell were averaged. The averaged spike for each cell was then used for principal component analysis and clustering to determine calcium clusters with *Seurat V4*.

Sarcomere analysis

Sarcomere analysis was performed as previously described.[64] Briefly, the α-actinin fluorescence image was segmented using the watershed segmentation method. Then the sarcomere organization score was calculated for each segmented cell using the Haralick correlation value, which is the correlation value of the co-occurrence matrix for given orientation and pixel pair offset distances. The height of the highest peak among all the orientation and pixel offset distances is defined as the sarcomere organization score for the cell.

In situ sequencing analysis

A customized computational pipeline was built with *MATLAB (2019b)* to decode gene identity and quantify the gene expression level of each cell from the *in situ* sequencing images. First, sequencing fluorescence images were preprocessed with top-hat filtering by a disk structuring element (radius = 3) to remove the background noise. Second, the contrast of the image for each channel from the second to fifth sequencing cycle was adjusted to match the image from the first cycle with histogram matching function *"imhistmatchn".* Third, the composite fluorescence images for the second to fifth cycle were registered with the composite fluorescence image from the first cycle using the phase correlation algorithm followed by local distortion registration with function *"imregdemons".* Fourth, the dots of amplicon locations were identified from images in the first cycle by a 3D regional maximum detection algorithm implemented in function *"imregionalmax".* Then the dominant color of every identified dot in each cycle was determined by a voxel volume surrounding its centroid location. The color sequence for each dot was decoded as a gene barcode and compared with the code-book. Fifth, cell segmentation was performed with ClusterMap,[29] then RNA reads were assigned to the segmented cells accordingly.

Python package *Scanpy*[54] was used for the single-cell gene expression analysis. Cells expressing less than 40 gene counts or only expressing three kinds of gene were filtered out. Gene counts of each cell were normalized so that the total count of all genes in each cell equaled the median number of total counts across all cells. The normalized count value was then log-transformed with log (x+1). *Combat*[55] was used to remove the potential batch effect among different imaging positions. Each gene in the cell-by-gene matrix was scaled to unit variance and zero mean followed by dimensionality reduction with principal components analysis (PCA). Based on the explained variance ratio, the top principal-components were used to construct the k nearest neighbor (kNN) graph for Leiden clustering.[30] UMAP[28] was used to visualize the 2D representation of each cell. *Monocle 3*[37] was used to compute pseudotime along the cell trajectory.

Locating recorded hiPSC-CMs

We used a custom-built pipeline based on *scikit-image v0.19.2* and *opencv-python v4.5.5.64*.[59] Electrode position was located using the 3D electrode image collected by reflection-mode and bright-field imaging and identified by the E-barcode positions. The electrode position in x and y coordinates was determined by the following steps: the electrode image was first projected to the x-y plane by maximum intensity projection (MIP) and transferred to gray-scale (pixel value ranging from 0-255). Then the MIP image was filtered with a global threshold of 50 to remove the non-electrode background. A 201-by-201 pixel size gaussian filter was applied to adaptively filter out the non-circular area, which is the interconnect of the electrode. After locating the electrode in the x-y plane,

the z coordinate of the electrode position was determined by fitting a 2D linear plane surface. The electrically recorded cell was further determined by calculating the area of intersection between each neighborhood hiPSC-CM and the electrode. The cell with the largest intersection area was identified as the electrically recorded cell. For hiPSC-CM samples, we used (i) high-density electrode arrays (electrode-to-electrode distance of 60 μm) to record 47% ± 6% of hiPSC-CMs and (ii) sparsely distributed electrode arrays (electrode-to-electrode distance of 480 μm) to record 3.4% ± 0.9% of hiPSC-CMs. In our system, 12% of electrodes were in contact with multiple cells, 53% of electrodes were in contact with single cells, and 35% of electrodes were in contact with small cell fragments or had no contact with cells.

hiPSC-CM electrophysiology data processing

We followed the procedure of *SpikeInterface v0.9*[58] to detect the spikes which passed the threshold in one channel. Each spike has a fixed length of 1.6 second with the sampling rate of 10 kHz. After spike detection, the spikes were aligned at the minimum of the corresponding spike dv/dt, and then averaged to get a spike representation of that channel.

For each spike representation, we first denoised the spike with wavelet denoising using *PyWavelets v1.1.0*.[56] Then, the spike features were extracted through two cycles of down sampling operations. We first down sampled the whole 1.6 second length spike to 22 points (zoomed-out binning) and then down sampled the 0.15 second length spike near the minimum of the differentiated spike to 40 points (zoomed-in binning). In total, we generated 62 feature points for each spike representation of each channel.

Spike sorting

Neural patch electrical recordings were first bandpass filtered with the frequency range from 300 to 3,000 Hz. To obtain the spike waveforms, the spike detection threshold was set as 5 times of standard deviations away from the mean and the minimum time between spikes was set as 3 ms. Segments in a time window of 3 ms with 1 ms before the trough of the waveform and 2 ms after the trough were extracted. Spike sorting was then conducted with *MountainSort*[57] and *SpikeInterface*.[58]

Locating recorded neurons

To identify electrically recorded neurons, we computed the spatial average positions across channels that recorded the same neurons and weighted the components with the square of the average waveform amplitude of each channel.[31] For neuron samples, we used high-density electrode arrays (electrode-to-electrode distance of 60 μm) to record 82% ± 4% of neurons.

Weighted Nearest Neighbor (WNN)

The WNN,[36] *i.e. FindMultiModalNeighbors* function from *Seurat v4*, was used to integrate the gene expression and electrophysiology data collected by *in situ* electro-seq. The principal component dimensionality for gene expression and electrophysiology was set as 7 and 6 (the elbow point in PCA variance), respectively. k = 20 was used to find the k nearest neighbor and calculate the modality-specific weights. A WNN graph integrating information of electrophysiology and gene expression was then built for downstream analysis including joint clustering (Leiden),[30] UMAP joint visualization and pseudotime derivation (*Monocle3*).

Pseudotime analysis

We used the R package *Monocle3* for the pseudotime calculation of gene expression, electrophysiology features and the WNN joint representation described above. A set of hyperparameters (Euclidean distance ratio = 2, geodesic distance ratio = $^2/_3$, minimal branch length = 5) in function *learn-graph* was used to first learn a principal graph of development. The node at the position of earliest stage was manually chosen as the root of principal graph to finalize the trajectory. Then the function *order_cells* was used to calculate the pseudotime.

Sparse reduced-rank regression (RRR) model and bibiplot

For the sparse RRR analysis,[38] we used 62 electrophysiological features across all electrically recorded hiPSC-CMs. Both electrophysiological features and gene expression were normalized and z-scored as described above. In brief, sparse RRR finds a linear mapping of gene expression levels to a low-dimensional latent representation, from which the electrophysiological features are then inferred with another linear transformation. The results were visualized by paired and aligned electrophysiological biplot and transcriptional biplot. Each biplot is composed of dots and lines. Each dot in the biplot represents a cell with paired measurements, with the x and y coordinates respectively representing Components 1 and 2 values in the aligned electrophysiological and transcriptional space. Each line in the biplot represents an E feature or gene. The sparse RRR model selected a set of genes for visualization in the transcriptional biplot that best explains electrophysiological variability. The x and y coordinates of each line's tip in the biplot indicate the contribution of the corresponding E feature or gene to Component 1 and Component 2, respectively. Comparing the directions of lines between the electrophysiological and transcriptional biplot can suggest which E features are correlated with which genes (Figure 6C). In Figures S5K and S5L, cross-validation was done by using 10 folds, elastic net α-values 0.25, 0.5, 0.75, and 1.0, and λ-values from 0.2 to 6.0. In Figures 6C, a model with rank r = 5, ridge penalty (α = 0.5), and lasso penalty (λ = 1.5) was used to yield a selection of genes. Following the method,[35,38] we selected the most stable results from the sparse RRR analysis. Specifically, we run the sparse RRR in 100 repetitions, and only genes that appeared more than 50 times were selected for the downstream analysis.

We used 10 times repeated 10-fold cross-validation to tune the regularization strength (Figures S5K and S5L). The selected model chose genes with a 5-dimensional latent space and achieved a cross-validated R^2 of 0.2. The cross-validated correlation between the first two pairs of projections was 0.69 and 0.49, respectively. These first two components roughly separate CM groups by their days of differentiation. These different groups show distinct genes correlated with electrophysiology features.

Coupled autoencoder model

A coupled autoencoder[39,40] was used for cross-modal inference. Specifically, the following hyperparameters were used: latent loss weight =1, Adam optimizer with learning rate = 0.0001, batch size = 10, training epoch = 15, epoch step = 1000. The latent dimensionality was set to d = 2 in order to capture the variability in the dataset. The genes selected by the sparse RRR model, and all 62 electrophysiological features were used as inputs for the coupled autoencoder.

To validate the cross-modal inference performance of the coupled autoencoder, 5-fold cross-validation was applied. Cells collected on Day 12, Day 21, Day 46, and Day 64 were randomly divided into 5 equal subsets. The coupled autoencoder was trained on 4 of the 5 subsets (training data), and then evaluated on the remaining 1 subset (validation data). This process was repeated 5 times, with each subset serving as the validation data exactly once. The performance across all 5 iterations was then used as the overall performance in downstream evaluations.

After training the coupled autoencoder network, we applied the pre-trained coupled autoencoder to infer temporal gene expression change from the continuous electrical recording of the same sample (Figure 7G). Specifically, the electrical activity of a cardiac sample was measured by the embedded electrodes from Day 17 to Day 64 of differentiation. Then a temporal gene expression profile from Day 17 to Day 64 of differentiation was inferred.

To apply the pre-trained coupled autoencoder model to LMNA-mutant hiPSC-CMs, we used the gene expression changes in LMNA-mutant hiPSC-CMs from previously reported data[42] to infer the electrophysiological waveform (Figures 7H and 7I). Then, the inferred LMNA-mutant hiPSC-CM electrophysiological waveform was compared to the waveform of LMNA-mutant hiPSC-CMs measured by mesh electronics. Additionally, random shuffle was performed as a negative control to further demonstrate that the inference of LMNA-mutant hiPSC-CMs was not due to coincidence. The gene expression changes in LMNA-mutant hiPSC-CMs were randomly shuffled and then used as input to the trained coupled autoencoder. The random shuffle was repeated 10 times for statistical reliability. We acknowledge that the randomness in the neural network training may lead to slight differences in the results of sparse RRR and coupled autoencoder analyses.

QUANTIFICATION AND STATISTICAL ANALYSIS

Statistical analysis was performed by GraphPad Prism. The statistical details of experiments can be found in the figure legends. Significant difference between two samples was evaluated by One-Way ANOVA or unpaired two-sided Student's t test. $p < 0.05$ was considered as statistically significant. *, **, and *** indicate statistical significance at $p < 0.05$, $p < 0.01$, and $p < 0.001$, respectively.

Supplemental figures

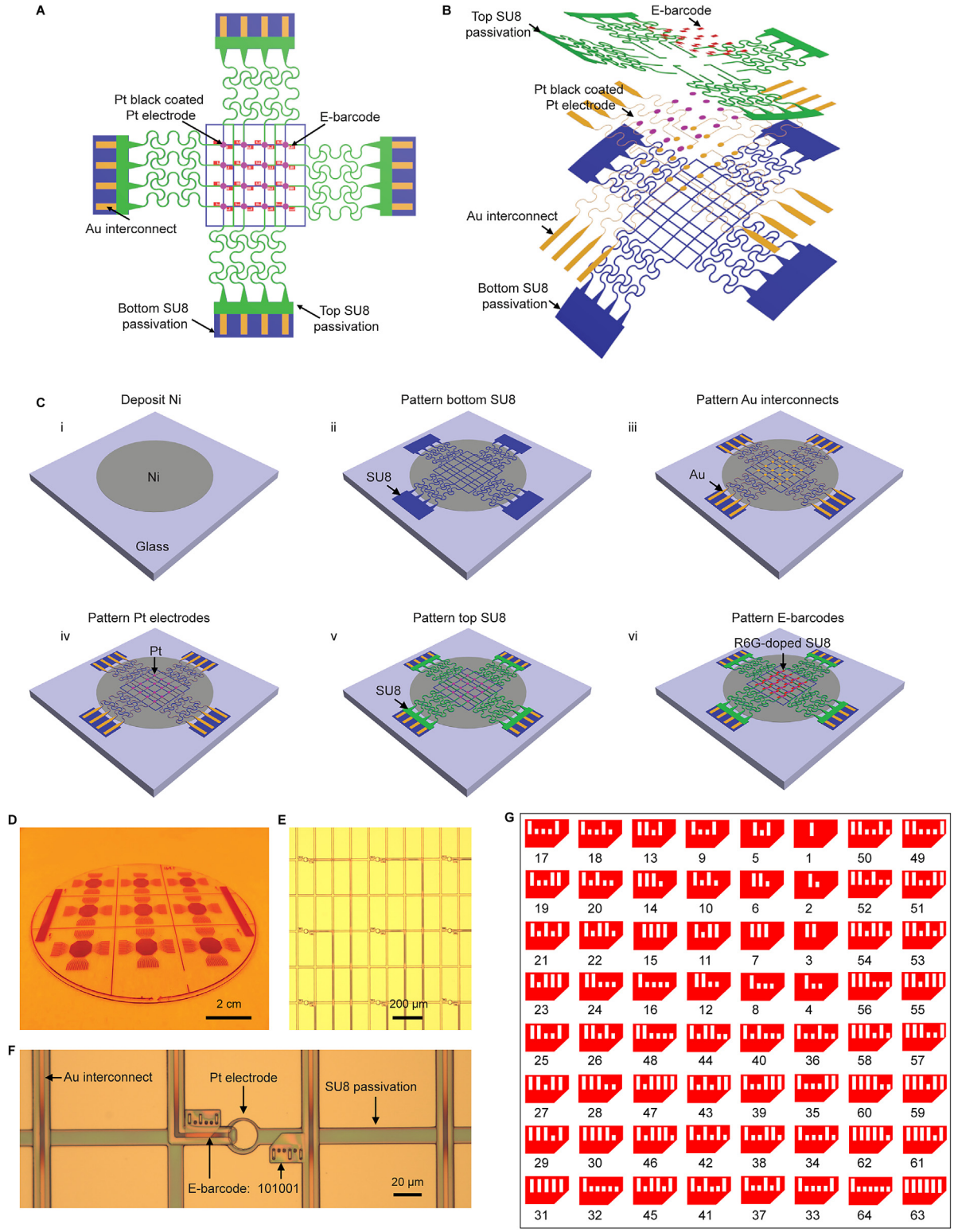

(legend on next page)

Figure S1. Design and fabrication of stretchable mesh electronics, related to Figure 1

(A) Top-view schematic of stretchable mesh electronics.

(B) Exploded-view schematic of different layers of stretchable mesh electronics.

(C) Schematics showing the key steps of the fabrication flow.

(D) Photograph of stretchable mesh electronics fabricated on a glass wafer.

(E) Bright-field (BF) optical image of a representative electrode array.

(F) BF image of a representative electrode with the paired E-barcodes and interconnects.

(G) Representative design of binary E-barcodes for labeling 64 electrodes.

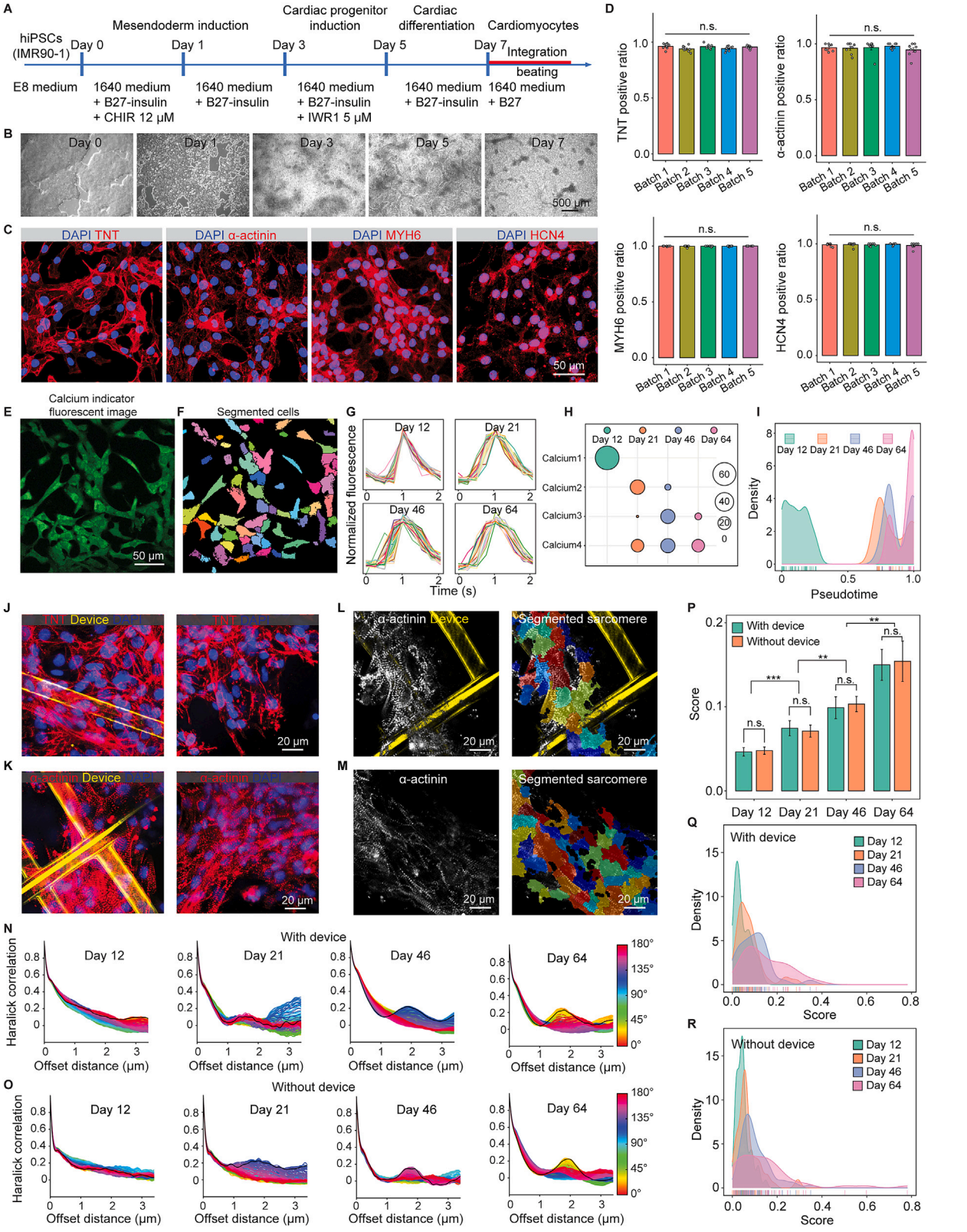

(legend on next page)

Figure S2. Human-induced pluripotent stem-cell-derived cardiomyocyte (hiPSC-CM) differentiation and integration with stretchable mesh electronics, related to Figure 2

(A) Schematics of the protocol for cardiac differentiation from hiPSCs.

(B) BF phase images showing the cell morphology at different differentiation days.

(C and D) Confocal fluorescence images (C) and corresponding statistical summary (D) of hiPSC-CMs at day 12 of differentiation. Values are mean ± SEM; n.s., not significant; one-way ANOVA test.

(E and F) Fluorescence calcium image (E) and corresponding cell-segmented image (F) of hiPSC-CMs.

(G) Averaged spikes of calcium signal traces of hiPSC-CMs at different differentiation days.

(H) Comparison of calcium clusters and differentiation days by dot plot.

(I) Distribution plots of pseudotime distributions of all the segmented hiPSC-CMs.

(J and K) Confocal fluorescence images of representative hiPSC-CM patch-electronics hybrids and hiPSC-CM patches.

(L and M) Fluorescence (left panels) and segmented (right panels) images of sarcomeres in representative hiPSC-CM patches with (L) and without (M) the device embedding.

(N and O) Haralick correlation computed at multiple offset distances and angles to determine the sarcomere organization score in the hiPSC-CM patches with (N) and without (O) devices.

(P) Barplots of sarcomere organization score in the hiPSC-CM patches. Values are mean ± SEM; n.s., not significant; ** $p < 0.01$, *** $p < 0.001$, two-tailed, unpaired t test.

(Q and R) Distribution plots of sarcomere organization score in the hiPSC-CM patches with (Q) and without (R) devices.

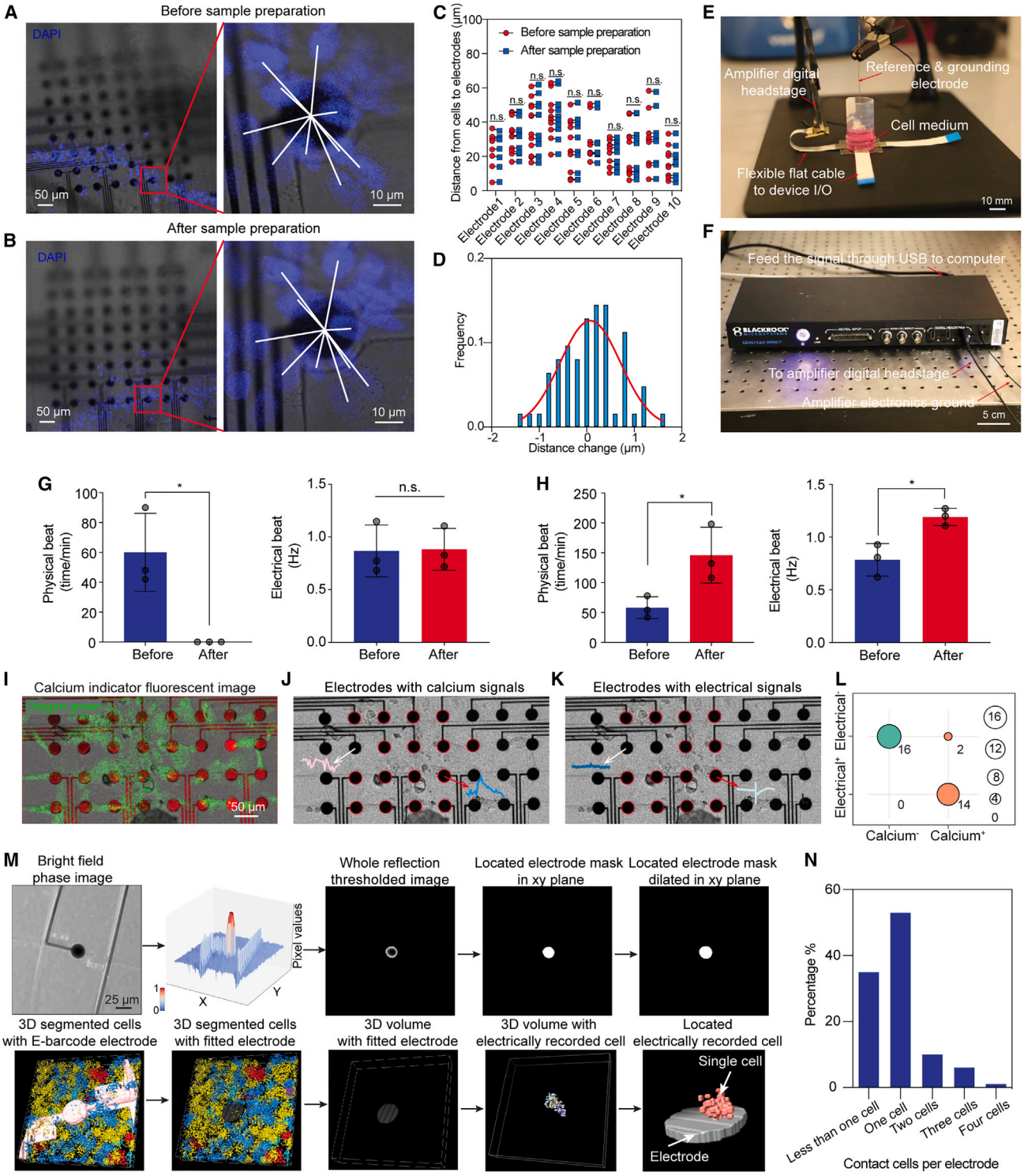

Figure S3. Electrical recording platform and measurement of hiPSC-CM patches, related to Figure 2

(A and B) Overlapped BF and fluorescence imaging of the same representative hiPSC-CM patch-electronics hybrid before (A) and after (B) the sample preparation. The zoomed-in view of the fluorescent image shows a representative electrode and its surrounding cells.

(C) Statistical summary of cell-to-electrode distances from the center of the DAPI signal to the center of the electrode. n.s., not significant; paired, t test.

(D) Probability distribution of the distance change after sample preparation.

(E and F) Photographs of the cell culture chamber connection (E) and Blackrock CerePlex direct voltage amplifier (F) showing the multiplexing recording setup.

(legend continued on next page)

(G and H) Statistical summaries of the physical and electrical beating rates of hiPSC-CM patch-electronics hybrids before and after blebbistatin and norepinephrine treatment. Values are mean ± SD; n = 3; n.s. not significant; * $p < 0.05$, two-tailed, unpaired t test.
(I) Overlapped BF and calcium imaging of hiPSC-CMs embedded with the electrode array.
(J) Red circles highlighting the electrodes overlapped by cells that show positive calcium signals.
(K) Red circles highlighting the electrodes that record positive electrical signals.
(L) Comparison of the calcium and electrical signals by dot plot.
(M) Schematics illustrating the computational pipeline to automatically identify hiPSC-CMs that directly contact the electrode as electrically recorded cell. Schematics for the multi-cell analysis (Figure S6A) is also generated from the same dataset.
(N) Statistical summary of contact cells per electrode.

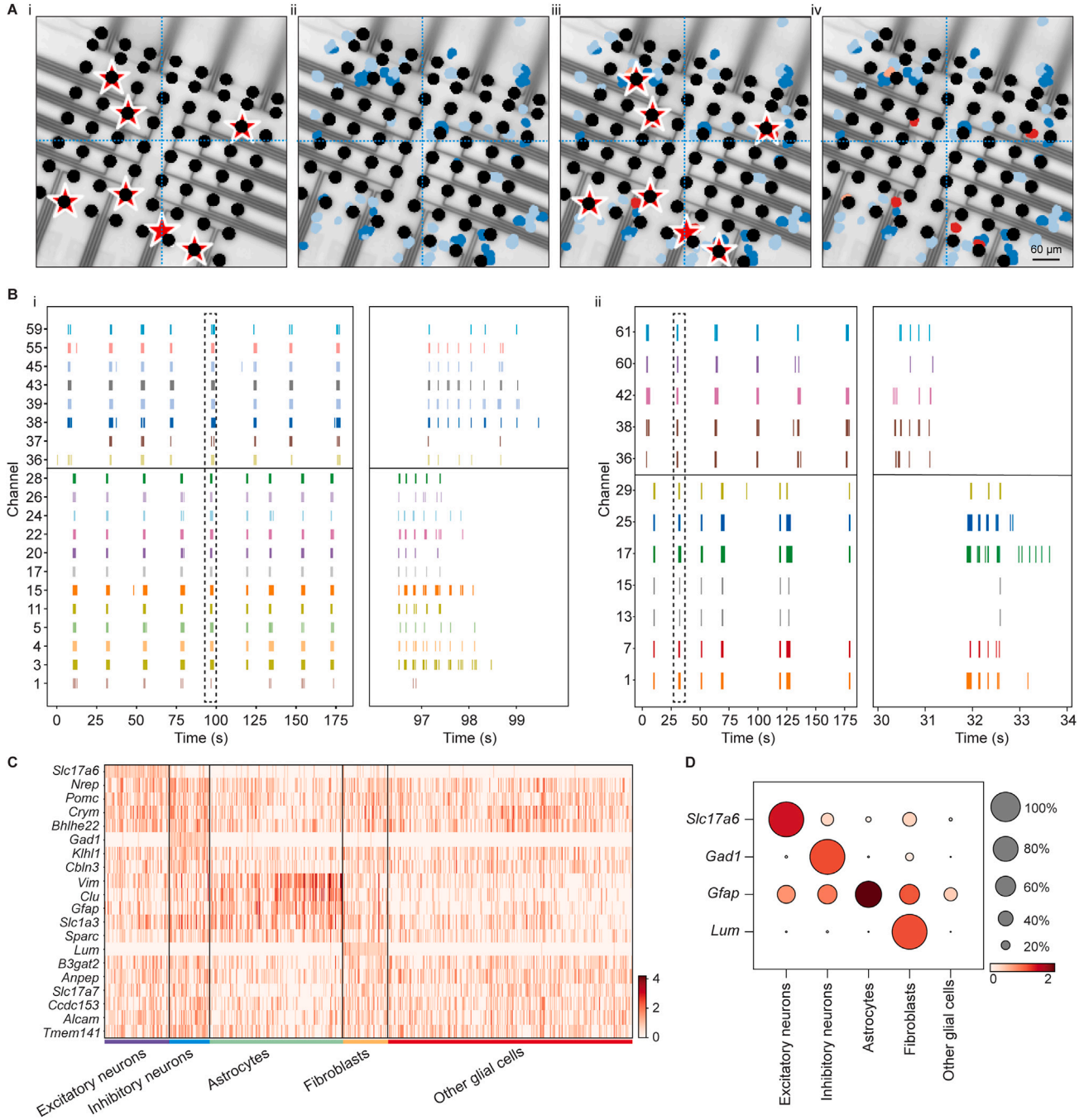

Figure S4. *In situ* electro-seq of neural patches, related to Figure 3

(A) Representative images showing the estimated neuron positions (red stars in i and iii) and finally determined electrically recorded neurons (red cells in iii and iv). All neurons near the device are labeled with blue dots. Dashed lines highlight the stitching boundaries of each imaging tile.

(B) Representative raster plots showing spike trains (left panel) and zoomed-in views of individual spikes (right panel) of two additional biological replicates, as the sample in Figure 3C.

(C) Heatmap of differentially expressed genes aligned with each cell cluster.

(D) Dot plot of selected marker gene expressions in neural patches.

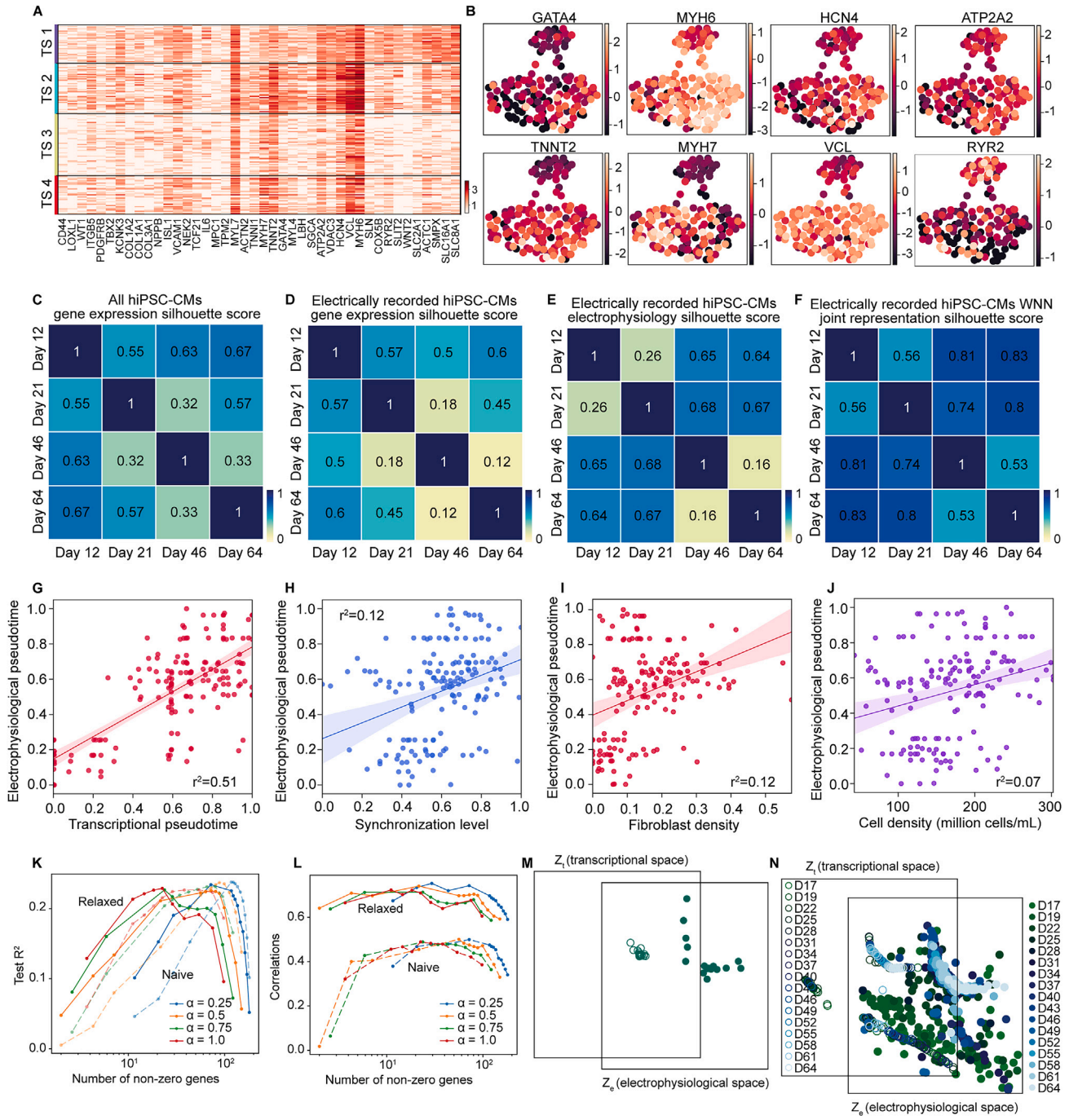

Figure S5. *In situ* electro-seq of hiPSC-CM development, related to Figures 4, 5, 6, and 7

(A) Heatmap of normalized differentially expressed genes aligned with each cell cluster.

(B) UMAP visualizations showing hiPSC-CM marker gene expressions.

(C–F) Matrix of silhouette scores measuring the separability of electrically recorded hiPSC-CMs. Gene expression of all hiPSC-CMs (C). Gene expression of electrically recorded hiPSC-CMs (D). Electrophysiology of electrically recorded hiPSC-CMs (E). WNN joint representations from gene expression and electrophysiology of electrically recorded hiPSC-CMs (F).

(G–J) Correlation of electrophysiological pseudotime with transcriptional pseudotime (G), hiPSC-CM synchronization level (H), fibroblast density (I), and cell density (J).

(K) Test R^2 of "relaxed" and "naive" sparse reduced-rank regression (RRR) analysis.

(L) Cross-validated correlations of relaxed and naive sparse RRR analysis.

(legend continued on next page)

(M) Coupled autoencoder-encoded 2D representations of a day 64 sample replicate. *Zt* (circles) and *Ze* (dots) represent the distribution of transcriptional and electrophysiological data, respectively.
(N) Coupled autoencoder-encoded 2D representation showing the distribution of electrophysiological data from a continuous electrical recording of the same cardiac patch (*Ze*, dots; bottom panel) and corresponding cross-modal inferred gene expressions (*Zt*, circles; top panel).

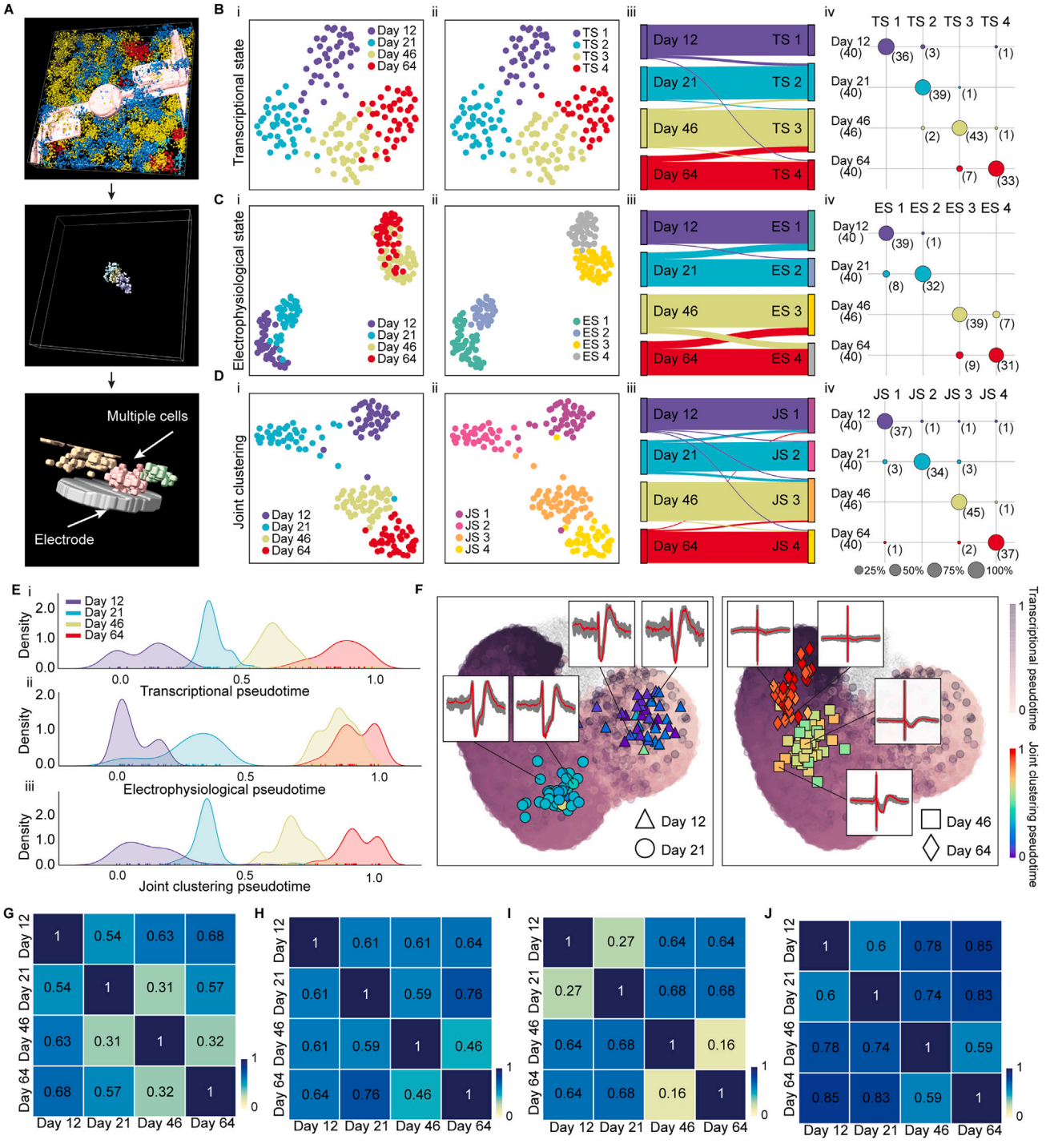

Figure S6. *In situ* electro-seq enables joint clustering of cell states by multiple contact cell analysis in hiPSC-CM development, related to Figure 5

(A) Schematics showing how to identify all the cells contacting the electrode for the multi-cell analysis.

(B) hiPSC-CM transcriptional states (t-states, TS) defined by gene expression. UMAP visualization of the gene expression from hiPSC-CMs that are color-coded by differentiation days (i) and t-states defined by Leiden clustering (ii). Comparison of t-states and differentiation days by river plot (iii) and dot plot (iv).

(C) hiPSC-CM electrophysiological states (e-states, ES) defined by electrophysiology and analyzed in the same way as in (B).

(D) hiPSC-CM transcriptional and electrophysiological joint states (j-states, JS) defined by weighted nearest neighbor (WNN)-integrated representations from gene expression and electrophysiology and analyzed in the same way as in (B).

(legend continued on next page)

(E) Distribution plots showing pseudotime distributions of all the electrically recorded hiPSC-CMs. Gene expression (i), electrophysiology (ii), and WNN-integrated representations of gene expression and electrophysiology (iii).
(F) Electrically recorded cells highlighted in the UMAP visualization of gene expression, with colors encoding joint pseudotime in (Eiii). Cells sequenced from all the samples across four stages are shown as gray embedding the same as Figure 4F. Insets show representative single-spike waveforms.
(G–J) Matrix of silhouette scores measuring the separability of electrically recorded multiple contact hiPSC-CMs. Gene expression of all hiPSC-CMs (G). Gene expression of electrically recorded hiPSC-CMs (H). Electrophysiology of electrically recorded hiPSC-CMs (I). WNN joint representations from gene expression and electrophysiology of electrically recorded hiPSC-CMs (J).

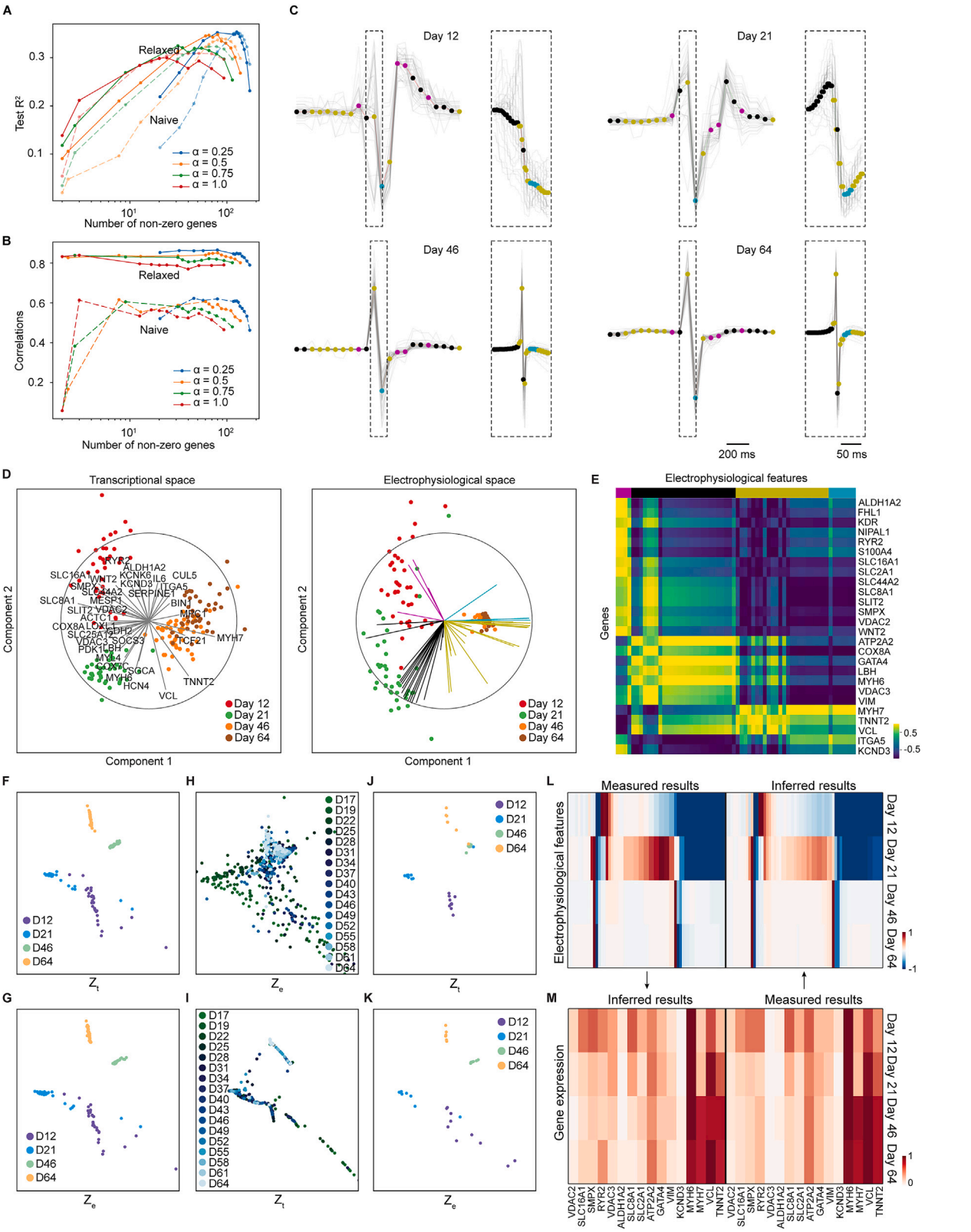

(legend on next page)

Figure S7. Cross-modal visualization, correlation, and inference of *in situ* electro-seq results of electrically recorded multiple contact hiPSC-CMs, related to Figures 6 and 7

(A) Test R^2 of relaxed and naive sparse RRR analysis.

(B) Cross-validated correlations of relaxed and naive sparse RRR analysis.

(C) Representative electrophysiological features extracted through downsampling of each spike waveform. 1.6-s waveforms are sampled in 22 bins. Inset shows 0.15-s fast spikes sampled in 40 bins.

(D) Sparse RRR model that visualizes and aligns transcriptional states (t-states) and electrophysiological states (e-states).

(E) Heatmap showing the correlation calculated by cosine distance between electrophysiological waveform features and genes from the sparse RRR analysis.

(F and G) Coupled autoencoder-encoded 2D representations of transcriptional (*Zt*, F) and electrophysiological (*Ze*, G) data trained by *in situ* electro-seq data.

(H and I) Coupled autoencoder-encoded 2D representations showing the distribution of electrophysiological data from continuous electrical recording (*Ze*, H) and the corresponding cross-modal inferred gene expressions (*Zt*, I).

(J and K) Coupled autoencoder-encoded 2D representations showing transcriptional data (J) and electrophysiological data (K) from samples across four developmental stages.

(L and M) Heatmap of transcript-to-electrophysiology (T-to-E) inference and electrophysiology-to-transcript (E-to-T) inference from the coupled autoencoder.